Biosensing Based on Localized Surface Plasmon Resonance of Gold Nanostructures Fabricated by a Novel Nanosphere Lithography Technique

Farah Fida

A Thesis

in

The Department

of

Electrical and Computer Engineering

Presented in Partial Fulfillment of the Requirements
For the Degree of Masters of Applied Science
(Electrical and Computer Engineering) at
Concordia University
Montreal, Quebec, Canada

December 2008

Your file Votre référence
ISBN: 978-0-494-63232-1
Our file Notre référence
ISBN: 978-0-494-63232-1

ABSTRACT

Biosensing Based on Localized Surface Plasmon Resonance of Gold Nanostructures Fabricated by a Novel Nanosphere Lithography Technique

Farah Fida

New gold nanostructures were prepared through a modified nanosphere lithography method. The structures, obtained by self-assembly of polystyrene microspheres and gold colloids in multilayers and subsequent removal of polystyrene, consist of nanohole/nanorings, distributed uniformly among gold nanoparticles on a silanized glass substrate. The size of the hole corresponds to the footprint of the polystyrene microspheres that were in contact with the glass substrate before dissolution. Sensing is based on the spectral measurement (in transmission mode) of the position of the Au localized surface plasmon resonance band in the ultraviolet-visible (UV-Vis) spectrum. Experiments were conducted with small molecules as well as with proteins (fibrinogen, Amyloid β-derived diffusible ligands (ADDLs), and AT5G07010.1, a plant protein from Arabidopsis thaliana) incubated on a functionalized substrate and have shown a higher sensitivity for platforms with 100 and 200 nm holes, compared to those having larger (500 and 700 nm) holes; for example, by using a platform with 100 nm holes, a concentration as low as 4.3×10^{-7} M of the plant protein (AT5G07010.1) could be detected. The biorecognition of the plant protein and the corresponding antibody has been shown by the broadening of the localized surface plasmon resonance band and the presence of a new band around 600-620 nm. It is believed that this band originates in interparticle localized surface plasmon resonance coupling, when biorecognition forces the functionalized particles into close proximity.

Acknowledgements

First I would like to thank my supervisor Professor Mojtaba Kahrizi, for giving me the opportunity and independence to pursue such an interesting thesis topic. Thank you for giving me the space to grow and learn in this domain.

I would also like to extend my sincere thanks to my co-supervisor Professor Vo-Van Truong for providing further insight into the theoretical aspect of this research. Thank you for your continuous support in helping me achieve my research goals.

I would like to extend my deepest appreciation to Dr. Simona Badilescu for her constant support and understanding. I do not have the words to express my gratitude in helping me get through the difficult times, and in encouraging me to strive to be a better researcher.

As I have no formal biological training, I would like to thank Professor Luc Varin for his guidance when it came time to investigating the biological aspect of this research work. Thank you for taking the time, and providing the necessary tools to complete my research.

Many thanks to Dr. Y. Djaoued from the Universite de Moncton, and special thanks to Mahmood Alimahmoodi of the Civil/Environmental Engineering department in always finding the time so that I could use the necessary equipment.

To my brother Karrar, thank you for your continuous support, and encouragement in getting through these last few years. Finally, I would like to thank my mother Zakia, and my late father Asghar Fida, for being such great role models, and for their unconditional love and support. You have always inspired me to strive for more, and I owe the success of this thesis to you.

Table of Contents

List of Figures

List of Tables

Chapter 1 : Introduction

Recent advances in noble metal nanostructures have led to the realization of increasingly complex structures of controlled size and shape such as, shells, rings, disks, cubes, etc. The optical response of a particular nanoscaled metal object, i.e. the dependence of the surface plasmon resonance (SPR) energy upon the size, shape and the dielectric environment, has been widely studied [1, 2, 3, 4,5].

Applications include biological and chemical sensing, Surface-Enhanced Raman scattering (SERS), near-field microscopy, bioimaging, etc. An accurate control of the surface topology is important, especially for biomedical applications. Larsson et al. [6] have fabricated nanorings by a template assisted method and used the structure for the detection of biological molecules in an aqueous environment. In this method, as well as in previous methods of preparation of ring-like gold structures, a monolayer of polystyrene (PS) is first deposited and gold is evaporated or sputtered into the interstices, through the polystyrene spheres mask [7, 8, 9, 10, 11, 12, 13, 14].

Although the SPR methods have in the past decade made important contributions to the quantification of biomolecular binding events, the optics associated with the conventional SPR reflectometry (e.g., in the Biacore commercial sensor) makes difficult device implementation. To overcome the drawbacks of SPR reflectometry and to enhance the sensitivity and detection limits, several groups have fabricated and characterized SPR biosensors in a planar, chip-based format using gold nanoparticles immobilized on optically transparent substrates in order to be able to work in transmission (or absorbance) mode [15, 16, 17, 18, 19]. In fact Rubinstein et al. worked with very thin (island) gold films (less than 10 nm thickness) which lead to the coining of the term Transmission Surface Plasmon Resonance (T-SPR); since the thickness of these films were so small they worked in transmission mode [20, 21,22]. Although the

absolute sensitivity to refractive index variations is smaller than that obtained using the Kretchmann configuration (The Kretchmann configuration is based on attenuated total reflection (ATR) at the interface of a gold layer and the prism, and it is used in commercial instruments), it has been shown that nanoparticle-based SPR instruments may provide a better resolution in addition to other advantages than the typical SPR devices [15, 16, 17].

The focus of this research is to develop a localized surface plasmon resonance (LSPR) biosensor using gold colloid-based nanohole- and nanoring structures fabricated through novel nanosphere lithographic (NSL) technique. In comparison with the classical NSL methods pioneered and developed by Van Duyne and colleagues (see for example [23, 24, 25, 26]) that involve depositing a polystyrene monolayer mask and then evaporating gold or silver into its interstices, this technique is based on the simultaneous assembly of polystyrene (PS) microspheres and of gold nanoparticles in multilayers by a vertical deposition method developed by our group [27, 28]. This sensor platform also provides a rapid detection mechanisms, something which is required in today's world of medicine. As the world of biomedical engineering continues to grow innovative biosensors will become increasingly in demand, in order to fulfill the needs of this domain.

In addition to the above mentioned, the aim of this research is to demonstrate that the gold nanostructures (holes and rings) prepared with a modified nanolithography method can function as the sensing platform of an optical biosensor. Research was conducted in order to determine their ability to provide information on the binding affinity of biomolecules. Biomolecules that were investigated as part of this work were fibrinogen, and amyloid β–derived diffusible ligands (ADDL). Furthermore, a model system was tested i.e. protein-antibody interaction (in our case a plant protein and its interaction with a rabbit polyclonal antibody) was investigated, to determine whether or

not the sensor platform would be able to behave in a specific manner i.e. to detect specific interactions. This interaction is quite important since antibody-antigen interactions are used extensively to study gene expression at the tissue and cellular level. Also, protein and antibody arrays can play a key role in the search for disease-specific proteins that have medical, diagnostic, and commercial potential as disease markers or as drug targets. Furthermore, micro-Raman spectroscopy measurements were also used to assess the SERS properties of the gold nanostructures. In order to evaluate the SERS properties, marine biotoxin samples (Saxitoxins, STX) were used.

Chapter 2 will discuss the theoretical background and will focus on the following; sensing/biosensing with noble metal nanoparticles and the LSPR phenomenon, the Mie theory, and comparisons between SPR and LSPR sensors. This chapter also discusses some details regarding the biomolecules that were used during the course of this study, protein and solid substrate interactions, as well as a brief theory behind the detection of antigen-antibody interaction. Chapter 3 focuses on characterization methods and measurements used in this work, i.e. scanning electron microscopy (SEM), ultraviolet-visible (UV-Vis) spectrophotometry, X-Ray diffraction (XRD), and Micro-Raman spectroscopy. Chapter 4 details the fabrication of the samples, it discusses the substrate preparation, the preparation of the gold and polystyrene composite, the functionalization of the sensor platform, and preparation of the biomolecules, as well as the protein and antibody deposition. Chapter 5 will focus on the results and discussion. It covers the structural, morphological and optical properties of the sensor platform. The sensitivity of the sensors along with the results on the biomolecular interaction, and Raman characteristics have also been detailed in this chapter. Finally, a summary of the findings as well as the future work, and contributions have been provided in the conclusion.

Chapter 2 : Theoretical Considerations

2.1 Sensing with Noble Metal Nanostructures and Modelling the Optical Properties of Noble Metal Nanoparticles

The intense scattering absorption of light from noble metal nanoparticles is the source of some of the beautiful colours in stained glass windows, and has attracted the interest of many scientists over decades in understanding this phenomenon. These nanoparticles exhibit a strong UV-Vis absorption band called SPR that is not present in the spectrum of bulk metals. Scientists have also learned that the shades produced by these noble metal nanoparticle suspensions are due to their interaction with light. In addition to this, with the advances in the nanoparticle optics domain, there is a better understanding of the relationship between properties (such as shape and size) and the observed colour of a metal suspension. Furthermore, since nanostructures have tuneable optical properties, they can be applied as materials for surface enhanced spectroscopies, optical filters, plasmonic devices and sensors [29].

Nanoparticles and nanoscale materials have proven to be useful especially for biological uses [29]. A biosensor can be generally defined as a device that consists of biological recognition system, often called a bioreceptor, and a transducer. The interaction of the analyte with the bioreceptor is designed to produce an effect measurable by the transducer, which converts the information into a measureable effect, such as an electrical signal. Figure 2.1 depicts the conceptual principle of the biosensing process. Biosensors that include transducers based on integrated circuit microchips are often referred to as biochips. In general, a biochip may consist of an array of individual biosensors that can be individually monitored and are used for the analysis of multiple analytes [30].

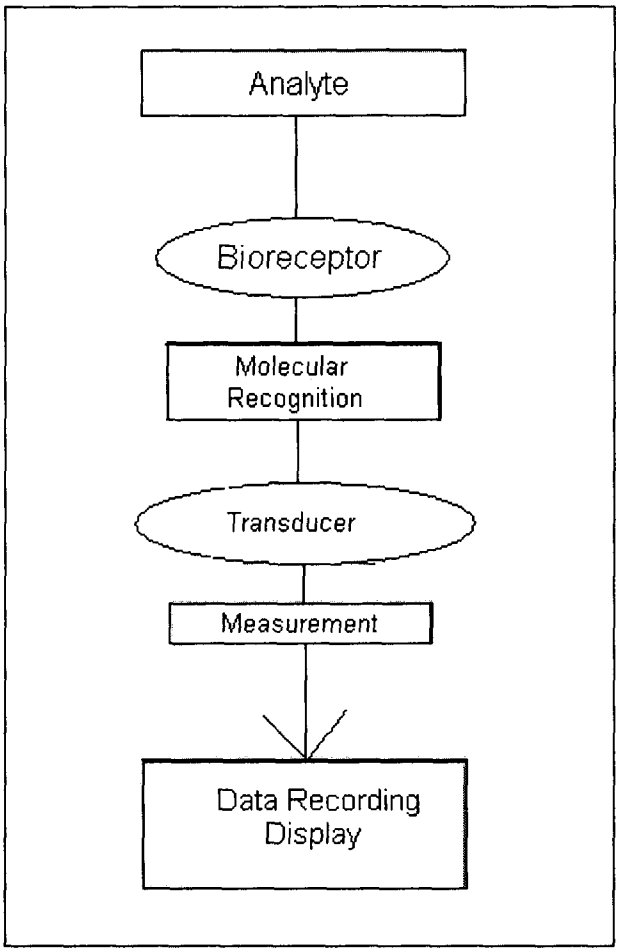

Figure 2.1: Biosensing Principle [30]

Nanoscale materials hold a particular interest to those in the biological sciences due to the fact that they are on the same size scale as biological macromolecules, proteins and nucleic acids. The interactions between biomolecules and nanomaterials have formed the basis for a number of applications e.g. potential therapeutic agents, cell tagging and sorting etc... Noble metal nanoparticles are especially interesting due to their unique optical properties which arise from their ability to support surface plasmons [29].

A surface plasmon (SP) is a charge density wave that exists at the interface between a metal and a dielectric. To excite SP optically, the momentum and the energy of an incident photon should match that of a plasmon; this is known as the resonance

condition. Light energy can then be coupled to a SP wave which results in a strong absorption at a certain wavelength, and angle of incidence. There are two types of measurement techniques:

- Measuring absorption as a function of incident angle (also known as the angular method)
- Measuring absorption as a function of incident wavelength (also known as the spectral method).

In the angular method it is essential to choose the correct wavelength, and metal. In the spectral method the incident angle must be controlled accurately; within 0.0001^0, it is also necessary to control the ambient temperature in this method. Our research made use of the spectral method [31].

Furthermore, noble metal particles (Au, Ag) exhibit strong UV-visible absorption, an effect known as localized surface plasmon resonance (LSPR). LSPR can be considered as a type of optical enhancement facilitated by the action of nanoparticles and microactivities [31].

LSPR also refers to the ability of the conduction electrons in the nanoparticle to oscillate collectively, which induces electromagnetic fields surrounding the nanoparticle and which determines the sensing volume in which refractive index based sensing can occur. Figure 2.2 depicts localized surface plasmon resonance in a colloidal gold sphere.

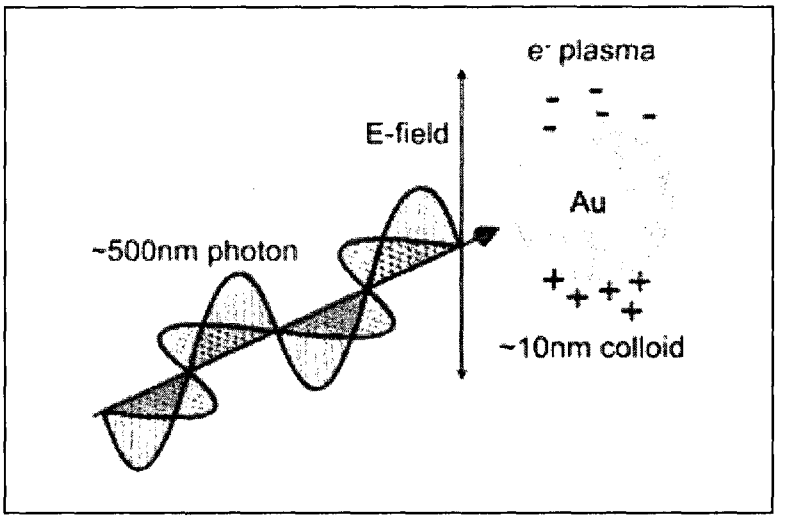

Figure 2.2: LSPR in colloidal gold - When the particle is smaller than the wavelength, localized surface plasmons can be excited in nanoparticles independently on the incident angle and polarization of the light. [32]

Since conduction electrons oscillate collectively to only specific wavelengths of light, nanoparticles exhibit selective photon absorption, which can be easily monitored using ultraviolet –visible spectroscopy. Optical extinction (sum of absorbed and scattered light is measured) results when an incident photon is in resonance with the collective excitation of conductive electrons. The maximum extinction wavelength, λ_{max}, of the LSPR is dependant upon the composition, size, shape and interparticle spacing of the nanoparticles as well as the dielectric properties of their local environment (i.e. substrate, solvent, and surface-confined molecules) [33].

Optimization of the LSPR sensor has been achieved by adjusting the size and shape of the nanoparticles. Studies have indicated that there are areas of heightened electromagnetic field strength located at the corners of the nanoparticles, as well as an overall tunable sensing volume that was determined by the average induced electromagnetic fields that surround the nanoparticles [33].

Compared with the conventional SPR biosensor, LSPR based sensors (due to the fact that we are working with nanoparticles) exhibit unique properties, including

faster response times, smaller pixel size, higher spatial resolution, and simultaneous surface-enhanced Raman scattering [31].

The presence of surface plasmon resonance (SPR) was demonstrated by Kreschmann and Raether and Otto in the late 1960s by the method of attenuated total internal reflection [31]. In the 1980s Liedberg et al, and Nylander et al demonstrated gas detection and biological sensing by using SPR techniques [31]. SPR is a powerful tool for monitoring biological interactions (Biacore AB, Uppsala, Sweden – created the first SPR based bio sensor). It is noninvasive, i.e. the method does not alter the physical and chemical properties of the analyte, and free of dye labelling and produces results in real time. These properties offer a great number of applications in pharmaceutical, food, and biotech industries; it also reduces the development costs and the cycling period in screening biointeractions [31]. The principal interest in the use of SPR for biomedical research is that it provides a platform for monitoring molecular interactions and defining the characteristics of proteins in terms of their specificity of interactions with other molecules; the association and disassociation rates at which they interact and how tightly they bind to each other [34]. SPR biosensors have been applied primarily in the study of protein-protein interactions, antibody-antigen recognition, and DNA-protein interactions [31].

2.2 Theoretical Approach Mie Theory

Noble metal nanoparticles (e.g. gold, silver) display unique size, shape and composition dependant optical properties, as mentioned earlier in the chapter. For instance a solution of gold and silver nanoparticles with a diameter of 20 nm appears to be brilliant red and yellow respectively. Gold and silver belong to a family of "free" electron metals, which refers to the fact that they both have filled valence shells, however do not have a filled conduction band [35]. The colors exhibited by

nanoparticles of these metals arise due to the interaction of incident light with the "free" electrons, resulting in resonant excitation of an oscillating dipole [35].

As mentioned in the previous section there are differences between SPR and LSPR. In the case of surface plasmon propagation (Figure 2.3a), plasmons propagate in the x and y direction along the metal dielectric interface, and there is an evanescent decay in the z-direction. A shift in the plasmon resonance condition may be attributed to the interaction between the electromagnetic wave at the metal surface and a molecular surface layer of interest [36]. This shift may be measured as described in section 2.1. In the case of localized surface plasmons (Figure 2.3b), LSPR which refers to the frequency at which the plasmon oscillates around the nanoparticle is a result of the interaction of light with particles that are smaller than the incident wavelength. LSPR, much like SPR, is sensitive to changes in the local dielectric environment [36].

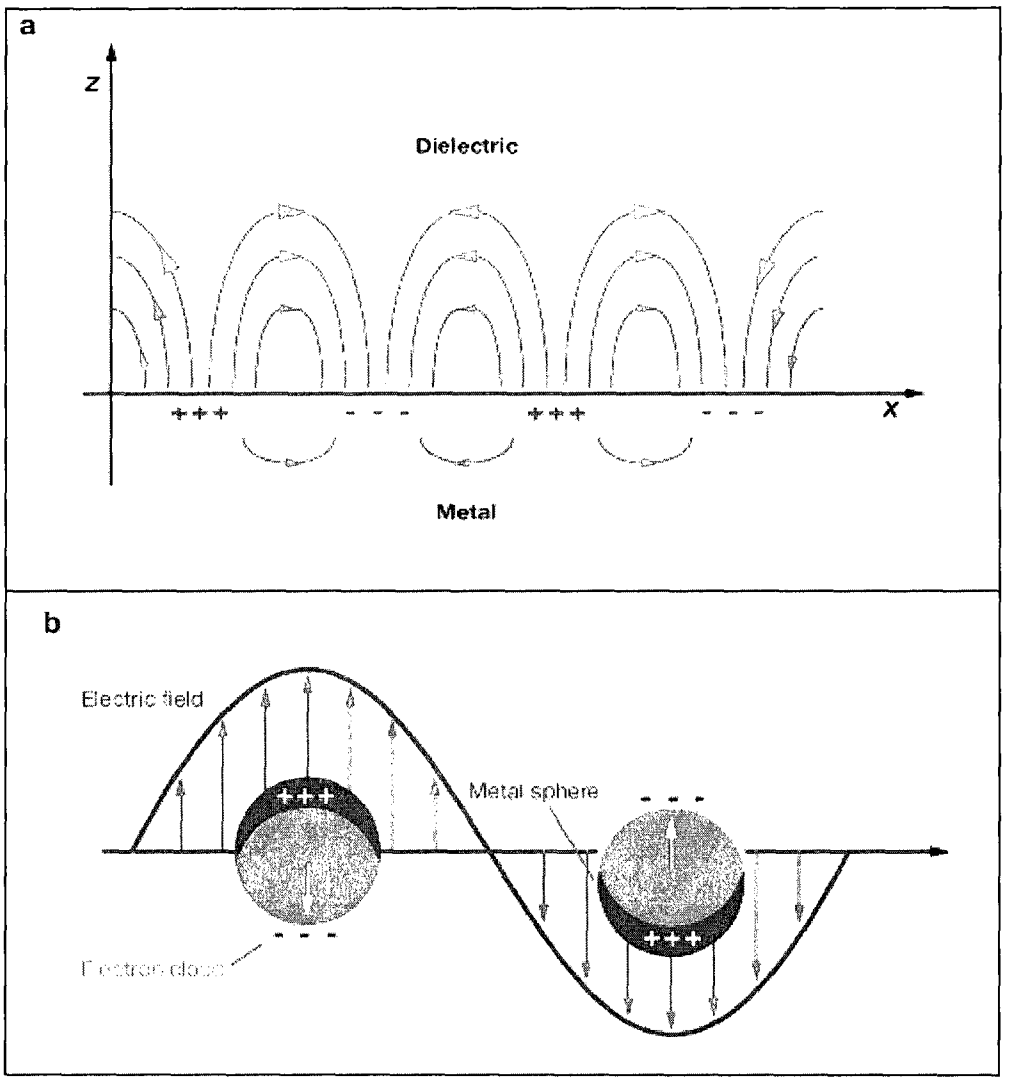

Figure 2.3: a) Surface Plasmon propagation; b) Localized surface plasmon [36]

The nanostructures prepared and used for biosensing in this work are defined as nanoparticle films which contain hole and ring structures. This kind of structure was not fabricated previously and, therefore, there is no theoretical description of it. However, because their structure and optical properties are closer to simple nanoparticle films than to nanohole (or ring) structures, the theoretical approach to best describe nanoparticle films is discussed below.

The established theorectical approach available for modelling the optical properties of a single nanoparticle is the Mie Theory [29]. Mie theory, also called Lorenz-Mie theory or Lorenz-Mie-Debye theory is a complete analytical solution of Maxwell's equations for the scattering of electromagnetic radiation by spherical particles (also called Mie scattering). The Mie solution is named after its developer German physicist Gustav Mie [37]. It should be noted that the Mie theory is only applicable to non-interacting particles i.e. particles that are spaced away from each other, well separated in their solid state. The interactions between nanoparticles in arrays are: near-field coupling e.g. in our samples the plasmon fields are close to one another, and far-field dipole interactions. These interactions are electrodynamic i.e. the dipole fields corresponding to Plasmon oscillations of a single particle, induces surface Plasmon oscillations in the adjacent particles [38]. The Mie theory estimates the extinction i.e. absorbance, or optical density, of a metallic sphere in the long wavelength, electrostatic dipole limit.

Consider a spherical nanoparticle for which radius is equal to a, that is irradiated by z-polarized light of wavelength λ (where $a << \lambda$; $a/\lambda << 0.1$). Using this limit, the magnitude of the electric field around the nanoparticle will appear to be static. This therefore allows us to solve Maxwell's equation (equation 2.1) using a quasi-static approximation, resulting in the following solution of electromagnetic field outside the particle (as depicted in figure 2.3b)

$$E_{out}(x,y,z) = E_o\hat{Z} - [(\varepsilon_{in} - \varepsilon_{out})/(\varepsilon_{in} + 2\varepsilon_{out})]\, a^3 E_o\, [(\hat{Z}/r^3) - (3z/r^5)(x\hat{x}+y\hat{y}+z\hat{Z})] \quad (2.1)$$

ε_{in} = dielectric constant of the metal nanoparticle

ε_{out} = dielectric constant of the external environment

Since ε_{in} is dependant upon wavelength the first term in square brackets (equation 2.1) determines the dielectric resonance condition for the particle. When the dielectric constant of the metal is roughly equal to $-2\varepsilon_{out}$, the electromagnetic field is enhanced relative to the incident field; for silver and gold, this condition is met in the visible region of the spectrum. The size (a) and external dielectric constant (ε_{out}) also play key roles in determining the electromagnetic field outside the particle [36].

Extinction is therefore defined by the equation 2.2:

$$E(\lambda) = [(24\pi^2 N_A a^3 \varepsilon_{out}^{3/2})/ \lambda \ln(10)] [\varepsilon_i(\lambda) /((\varepsilon_r(\lambda) + \chi\varepsilon_{out})^2 + \varepsilon_i(\lambda)^2)]] \quad (2.2)$$

$E(\lambda)$ = extinction which is in turn equal to the sum of absorption and Rayleigh scattering

N_A = the areal density of nanoparticles

a = the radius of the metallic nanosphere

ε_{out} = dielectric constant of the external environment - assumed to be a positive real number and wavelength independent

λ = wavelength of the absorbing radiation

χ = 2 for the case of a sphere - it can take on values as large as 20 to account for particle geometries with high aspect ratios.

$\varepsilon_i(\lambda)$ = imaginary portion of the metallic nanosphere's dielectric function

$\varepsilon_r(\lambda)$ = real portion of the metallic nanosphere's dielectric function

When the resonance term i.e. $(\varepsilon_r(\lambda) + 2\varepsilon_{out})^2$ from equation 2.2 approaches zero the LSPR condition is met.

The LSPR spectrum of an isolated metallic nanosphere embedded in an external dielectric medium will depend on the following:

- a the nanoparticle radius
- ε_i and ε_r the nanoparticle material

- ε_{OUT} the dielectric constant of the external environment

Furthermore, if the nanoparticles are not spherical in shape, as is the case in many real samples, the extinction spectrum will depend on the following nanoparticle characteristics:

- In plane diameter
- Out-of-plane height
- Shape

In this scenario, the resonance term i.e. $(\varepsilon_r(\lambda) + 2\varepsilon_{out})^2$ from equation 2.2 is replaced with the following:

$$(\varepsilon_r(\lambda) + \chi\varepsilon_{out})^2 \qquad (2.3)$$

The theoretical model by Mie was developed for spherical particles. An adaptation of this model for non-spherical particles shows an anisotropic distribution of surface plasmons around the particles resulting in shape-dependent absorption spectra.

For cases where the nanoparticles are not spherical as mentioned above e.g. nanorods, the plasmon resonance splits into low- and high-energy bands, The high-energy plasmon (transverse) corresponds to the electron oscillations perpendicular to the major axis (perpendicular to the length of rod), while the low-energy plasmon (longitudinal) results from the oscillations along the major axis (parallel to the length of the rod) [39].

In addition to this, when the nanoparticles are supported on a substrate, the LSPR is also dependant upon the following factor [29]:

- Substrate dielectric constant

In [40] the authors have found that the wavelength corresponding to the extinction maximum shifts to the red, with the increasing refractive index (n) of the substrate. Experimental spectra were modeled using the discrete dipole approximation (DDA).

DDA is a numerical solution for Maxwell's equations which can generate the absorption, scattering, and absorption cross sections for particles of arbitrary shape. The DDA results qualitatively predicted that the wavelength shifts to the red with increasing refractive index of the substrate. However the theory overestimates the sensitivity to n by approximately a factor of 2.

Further to the above stated, LSPR extinction (or scattering) wavelength maximum, λ_{max}, is sensitive to the dielectric constant ε (or refractive index, n; both are related by $\varepsilon = n^2$). Thus, changes in the local environment—such as through the presence of an adsorbed species — should cause a shift in λ_{max}, [36] which results in the following:

$$\Delta\lambda_{max} = m\Delta n\,[1 - \exp\,[-2d/l_d]] \qquad (2.4)$$

m = bulk refractive-index response of the nanoparticle(s)

n = the change in refractive index induced by the adsorbate

d = the effective adsorbate layer thickness

l_d = is the characteristic electromagnetic-field-decay length (approximated as an exponential decay).

This relationship is the basis of LSPR wavelength-shift sensing experiments.

LSPR excitation results in wavelength selective absorption due to the oscillation of collective conduction electrons to only specific wavelengths. This has been applied in nanosensors due to its ultrasensitive biodetection with simple, small, light and low-price instrumentation [41].

It has been shown by several groups that hole plasmon excitation is a highly localized resonance and that the peak in the extinction spectrum corresponds to the LSPR confined to the holes. The nanoparticles prepared through the methods described in the upcoming chapters, because of a lack of a continuous metal structure, can only support localized surface plasmons; each nanoparticle represents a source of localized excitation of surface plasmons.

2.3 Bioanalytical Detection and Optical Transduction Based on SPR (or LSPR)

A major challenge in cell and molecular biology research is to understand the relationship between the structural features of biological macromolecules and their function. An understanding of the mechanisms that control cellular processes requires knowledge of protein activities, and how the interactions and complex formation are regulated at specific sites and times in the cell [34].

Development of surface SPR biosensor has made kinetic analysis of most biomolecular interactions routinely accessible and permits the real-time analysis of reactions without the use of labels. Since SPR detection is independent of the chemical nature of the sample being analyzed, in principle all types of molecules such as proteins, lipids, nucleic acids and small molecules such as drugs, substrates and cofactors can be used to monitor biomolecular interactions [34].

The potential of SPR biosensors were realized in the early 1980s, when researchers were able to detect immunoglobulin antibodies by observing the change in critical angle when the antibodies bind selectively on to Au film. SPR sensors detect the local refractive index changes that occur when the target analyte binds to the metal film or nanoparticles. Since their inception, changes in the SPR chracteristics have been used in refractive-index-based sensing to detect analyte binding at or near a metal surface and has been widely used to monitor a broad range of analyte-surface binding interactions including the absorption of small molecules, ligand-receptor binding, protein adsorption on self-assembled monolayers, antibody-antigen binding, DNA and RNA hybridization and protein-DNA interactions. LSPR based sensors as mentioned previously exhibit unique properties, including faster response times, smaller pixel size, higher spatial resolution, and simultaneous surface-enhanced RAMAN scattering, and have been used for the same purposes as those described for the SPR sensors [29].

There are however several differences between SPR and LSPR sensors as detailed in table 2.1.

Feature/characteristic	SPR	LSPR
Label-free detection	yes	yes
Distance dependence	~1000nm	~30nm (size tuneable)
Refractive index sensitivity	2×10^6nm/RIU	2×10^2nm/RIU
Modes	angle shift wavelength shift imaging	extinction scattering imaging
Requires temperature control	yes	no
Chemical identification	SPR-Raman	LSPR-SERS
Field portability	no	no
Commercially available	yes	no
Commercial Cost	$150 000–$300 000	Estimated Cost - $5000 (multiple particles) $50 000 (single nanoparticle)
Spatial resolution	10×10 μm	nanoparticle
Nonspecific binding	minimal (determined by surface chemistry and rinsing)	minimal (determined by surface chemistry and rinsing
Real-time detection	scale = $10^{-1} - 10^3$ s, planar diff	time scale = $10^{-1} - 10^3$ s, raidal diffusion
Multiplexed capabilities	yes	yes - possible
Small molecule sensitivity	good	better
Microfluidics compatibility	yes	possible

Table 2.1: Comparison between SPR and LSPR sensors [29]

Some important differences to appreciate are that SPR sensors exhibit a large refractive index sensitivity ~2 x 10^6nm/RIU, whereas the LSPR nanosensor has a more modest refractive index sensitivity ~2 x 10^2nm/RIU. Since this number is four orders of magnitude less than that of the SPR sensor, initially it was assumed that the LSPR sensor would be 10,000 times less sensitive that the SPR sensor. This however is not the case, since the short and tuneable characteristic electromagnetic field decay length, l_d, (which is actually the depth of penetration of the evanescent wave into the material) provides the LSPR nanosensor with additional advantages. In the case of LSPR nanosensors results indicate that the decay length, l_d, is ~5-15nm or ~1-3% of the light's wavelength and depends upon the size, shape, and composition of the nanoparticles (as

opposed to the SPR sensor whose decay length is reported to be ~200-300 nm or ~15-25% of the light's wavelength for the SPR sensor).

Furthermore, no temperature control is required for the LSPR nanosensor due to its lower refractive index, whereas a SPR sensor does require this control due to its high refractive index; for every degree of temperature change there is a change in the refractive index. Finally the estimated cost associated to an LSPR system is less than $5000, whereas the cost associated to commercial SPR instruments may vary between $150,000-$300,000.

Another difference between SPR and LSPR, is that in SPR spectroscopy, the conventional ATR Kreschmann configuration is used for measurements, LSPR uses exctinction (or transmission) measurements. Figure 2.4 depicts the optical setup for extinction spectroscopy typically found in conventional spectrophotometers.

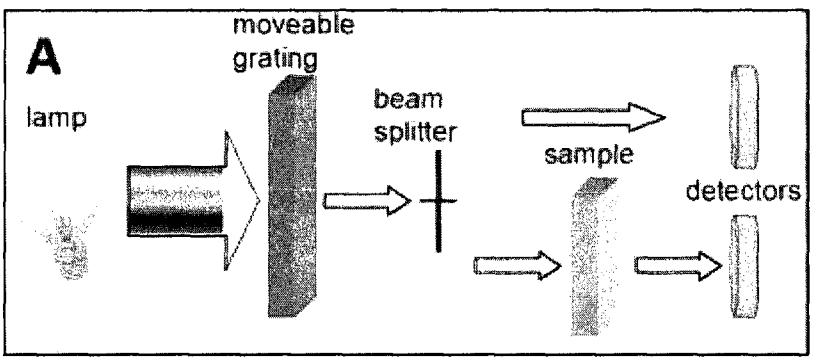

Figure 2.4: Optical Setup for Extinction Spectroscopy - A moveable grating (or prism) selects a narrow wavelength region from the white light of a lamp and a spectral scan is acquired by sequentially measuring intensity at different wavelengths. Also, as a second feature, a beam splitter generates a beam used for continuously calculating the reference spectrum. [32]

Although both sensors differ there is however a unifying relationship, i.e. the overall response of both of them may be described by the equation 2.3:

$$\Delta\lambda_{max} = m\Delta n \left(1 - \exp(-2d/l_d) \right) \qquad (2.3)$$

where,

$\Delta\lambda_{max}$ = wavelength shift response

m = refractve index sensitivity

Δn = change in the refractive index induced by an adsorbate

d = effective adsorbate layer thickness

l_d = characteristic electromagnetic field decay length

This equation predicts an adsorbate's effect on the sensor for planar SPR sensors. This exponential equation approximates the response for adsorbate layers and provides a fully quantitative explanation for the response for LSPR nanosensors. For both the LSPR and the SPR sensor, the sensitivity arises from the distance dependence of the average induced square of the electric fields that extend from the nanoparticles' surfaces [29].

2.4 Understanding Protein and Solid Substrate Interactions

Protein-substrate interaction is a point of interest in several domains e.g. molecular biology biomaterials, nanotechnology etc... In nanotechnology, for nanoSPR sensors, it is important to understand this interaction in order to analyze the biological/electronic junction. There is a high demand to understand in greater detail these types of interactions, therefore much effort has been put in protein adsorption experiments; in order to predict and understand the protein conformation, and the kinetic details of the protein-surface interaction [42].

Proteins are known to denature, i.e. a process in which proteins or nucleic acids lose their 3D-structure by application of some external stress or compound, or by adsorption at the liquid-solid or vapour-solid interface. Research indicates that proteins do retain most of their structure on electrostatically neutral hydrophilic surface i.e. adsorb well usually from water, as opposed to hydrophobic or charged surfaces. Kinetic effects, however, of this type of interaction may vary, since long term behaviour may differ from

short term behaviour. In addition to this, surface coverage of a protein will depend upon the rate at which the protein was introduced into the system. The overall behaviour of this type of interaction is dependant upon the type of protein and the surface being analyzed, and may also be attributed to the fact that the protein may undergo conformational changes [42].

While the direct observation of the atomic-scale surface morphology is impossible at the moment, there are however certain ways to isolate and obtain information about a particular region of a protein. One such method is called the time-to-flight secondary ion mass spectroscopy. In this technique, an adsorbed protein layer is bombarded with ions, breaking off short segments (as much as several peptides) from the upper nanometer of the adsorbed layer. After identifying these segments using mass spectroscopy, the orientation of the protein or its state of unfolding can be inferred [42]. This technique could be applied in theory to most proteins, at different interfaces to provide structural information [42].

2.4.1 Fibrinogen

As previously mentioned, Fibrinogen was used in order to test the sensitivity of our sensor. Fibrinogen is a soluble protein; it is abundantly present in plasma. Fibrinogen is a human plasma protein (340 kDa) well studied because of its biological importance in the blood coagulation cascade. It is synthesized in the liver and circulating in the blood at a concentration of 2.6 mg/mL. When tissue damage occurs, fibrinogen adsorbed to the wound is cleaved by another coagulation protein into an insoluble clot of fibrin. The most accepted model of fibrinogen was proposed by Hall and Slayter [43] in 1959; the total length of the molecule is about 47.5 nm. Fibrinogen levels reflect the clotting ability and activity in the body. Reduced concentrations of fibrinogen may impair the body's ability to form a stable blood clot. Fibrinogen concentrations may rise sharply in any condition that causes inflammation or tissue damage, such as acute infections,

cancer, coronary heart disease, myocardial infarction, stroke, rheumatoid arthritis, trauma etc... Fibrinogen consists of the following:

FIBRINOGEN $\Rightarrow$ FIBRIN MONOMER $\Rightarrow$ INSOLUBLE FIBRIN

(TROMBIN) (SELF-ASSOCIATION)

Human Fibrinogen is comprised of six polypeptide chains: 2 Aα, 2Bβ, and 2γ linked together by a disulfide bridge (the α, β, γ chains are depicted in figure 2.5) [44].

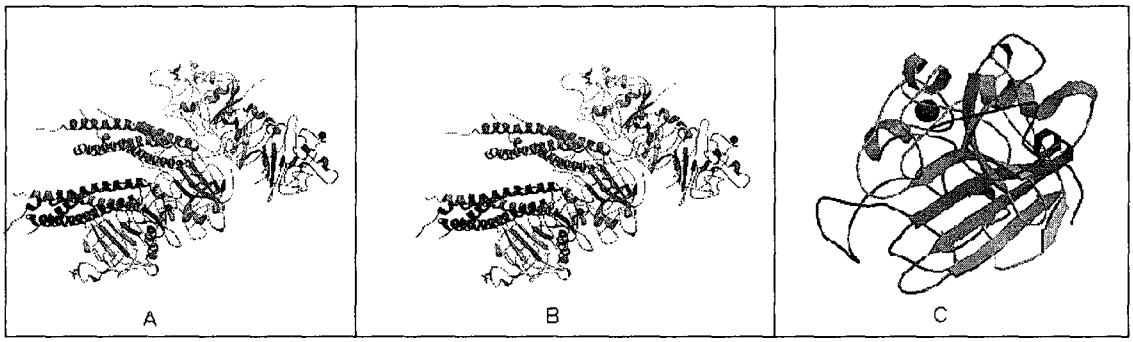

Figure 2.5: Structure of Human Fibrinogen – a) Alpha Fibrinogen Chain b) Beta Fibrinogen Chain c) Gamma Fibrinogen Chain [45]

2.4.2 ADDL

As previously stated, the detection of the disease marker polypeptide, ADDL, involved in the development of Alzheimer's disease was also investigated as part of this research project. Research indicates that ADDL is a biological molecule that may cause neurological dysfunctions relevant to memory. It is thought that they are associated with Alzheimer's disease. Alzheimer's disease is the leading cause of dementia in people over the age of 65. Although first characterised almost 100 years ago by Alois Alzheimer, the root cause of the disease is not understood and a precise diagnostic method is yet to be discovered.

There are however two inter-related theories for Alzheimer's disease which focus on the involvement of neurotoxic assemblies of a small 42-amino acid peptide known as amyloid beta (Aβ).

This hypothesis suggests that the amyloid plaques causes:

- *neuronal degeneration*
- memory loss
- progressive dementia

It is believed that, until the Aβ protein monomers (present in humans) assemble into amyloid fibrils, they are not toxic.

The other toxins are known as Aβ derived diffusible ligands ('ADDLs'), which are small, globular, and readily soluble, 3-24mers of the Aβ monomer and are potent. They are selective central nervous system neurotoxins. It is believed that they possibly inhibit mechanisms of synaptic information storage with great rapidity. Recent studies have indicated that ADDLs now have been confirmed to be greatly elevated in autopsied brains of Alzheimer's disease subjects. An ultrasensitive method for ADDLs/anti-ADDLs antibody detection potentially could emerge from LSPR nanosensor technology [29].

2.5 Detection of Antigen-Antibody Interaction and Feasibility of LSPR Biosensing with a Biological Couple.

Antigens are substances that prompt the generation of antibodies and can cause an immune response. An antibody is a complex biomolecule that consist of hundreds of individual amino acids arranged in a highly ordered sequence. Antibodies have specific binding capabilities for specific structures [30]. An antigen and its antigen specific antibody interact much like a lock and key i.e. specific geometrical configurations of a unique key will enable it to open a lock [30]. In much the same way, an antigen will only fit in with a particular antibody as depicted in figure 2.6.

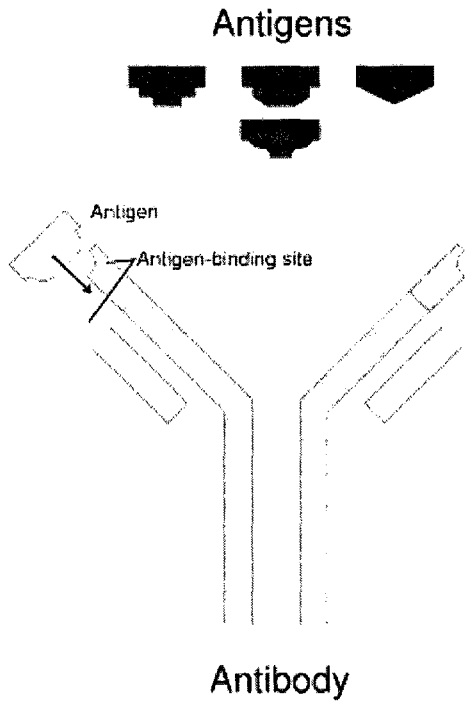

Figure 2.6: Antibody-Antigen interactions [46]

Antibodies are commonly used as bioreceptors for biosensors, and with the advent of label free detection methods, i.e. detection based on surface Plasmon resonance, one can monitor the binding events in real time without labeling [47]. As mentioned in earlier section of this chapter, the refractive index near the surface of the sensor changes when there is a reaction of any nature. In the case of the interaction of the antigen with its respective antibody, a change will result at the metal surface within the surface plasmon field and an increase in the LSPR signal should be observed. Since LSPR detection is independent of the chemical nature of the sample being analyzed, in theory proteins, nucleic acids etc... can be used to monitor biomolecular interactions. It should be noted that the interaction between the antigen and antibody is very specific [47].

Antibodies and antigen binding involves non-covalent bonding and is a reversible process. The rate of reaction is proportional to the concentrations of the reactants. One

can analyze the tightness of binding, i.e. "affinity", of a single antigen which binds to a single antibody's binding site by defining an equilibrium constant:

For the reaction: Ab + Ag = AbAg

- Ab = the free antibody
- Ag = the free antigen

The rate of formation of the AbAg complex may be defined by equation 2.4

$$k_{forward}\,[Ab][Ag] \qquad (2.4)$$

The rate at which it breaks down may be defined by equation 2.5

$$k_{backward}\,[AbAg] \qquad (2.5)$$

Square brackets represent concentration, and the rate constants i.e. k forward or backward depend upon the temperature and pH.

At equilibrium, an equilibrium or affinity constant K is defined by equation (2.6)

$$K = k_{forward} / k_{backward} = [AbAg]/[Ab][Ag] \qquad (2.6)$$

The concentration of [Ab] [Ag] will not equal the starting concentration as was used during the formation of the complex [AbAg] [48].

The reactions presented above are only for single binding sites, however in reality it is much more complex, as an antibody and antigen may have multiple binding sites (as in the case of cells). These numerous binding sites result in "extra tightness" which is referred to "avidity" or "functional affinity". This affinity is greater than a single site affinity.

In practice, when measuring the binding of an antibody to a cell surface antigen [48] the exact number of binding sites are not taken into consideration, rather an average "functional affinity" is determined. The functional affinity constant has an important bearing on the appropriate concentration of antibody needed for a particular application e.g. diagnostic assay or therapy [48].

As an antibody not only has multiple binding sites but there may also be n identical sites, to which a ligand may bind to. At a particular concentration, a ligand may bind to all these n sites. In this case, the number of bound ligand molecules per antibody molecule will equal n, the antibody valence.

Assuming if all binding sites are identical and independent, the binding reaction is represented by equation 2.7:

$$S + L = SL \qquad (2.7)$$

S = binding site on the antibody

L = ligand

The forward and backward reaction rates, at equilibrium, are represented by equation (2.8):

$$k_{forward}[S][L] = k_{backward}[SL] \qquad (2.8)$$

Where:

[SL] = concentration of occupied antibody sites

[S] = concentration of free sites

[L] = concentration of unbound ligand

The affinity of the antibody for the ligand K (L/mol) may be represented by equation 2.9 i.e. the ratio of the rate constants:

$$K = k_{forward} / k_{backward} = [SL] / [S][L] \qquad (2.9)$$

If the total concentration of ligand molecules [L]+[SL] and the total concentration of antibody sites [S]+[SL] are known, then K can be determined by measurement of any one term on the right side of equation

Chapter 3 : Characterization Methods and Measurements

In order to perform the necessary measurements, and characterization of the samples prepared throughout the course of this research project, several methods were used. They are the following:

- Scanning Electron Microscopy (SEM)
- UV-Vis Spectrophotometry
- X-Ray Diffraction (XRD)
- Micro-Raman Spectroscopy

3.1 Scanning Electron Microscopy

The Scanning Electron Microscope (SEM), as depicted in Figure 3.1, scans a sample with a beam of electrons that interact with the sample. When the surface of the sample is scanned in this manner it allows researchers to view the microstructural details of their object of study. Some of the electrons and other electrons generated during this process escape from the sample and reach a detector. The number of electrons that reach the detector at each point on the sample depends on the topology of the sample and the atomic weight of the atoms at the surface, and these variations in signal strength lead to image formation [49, 50].

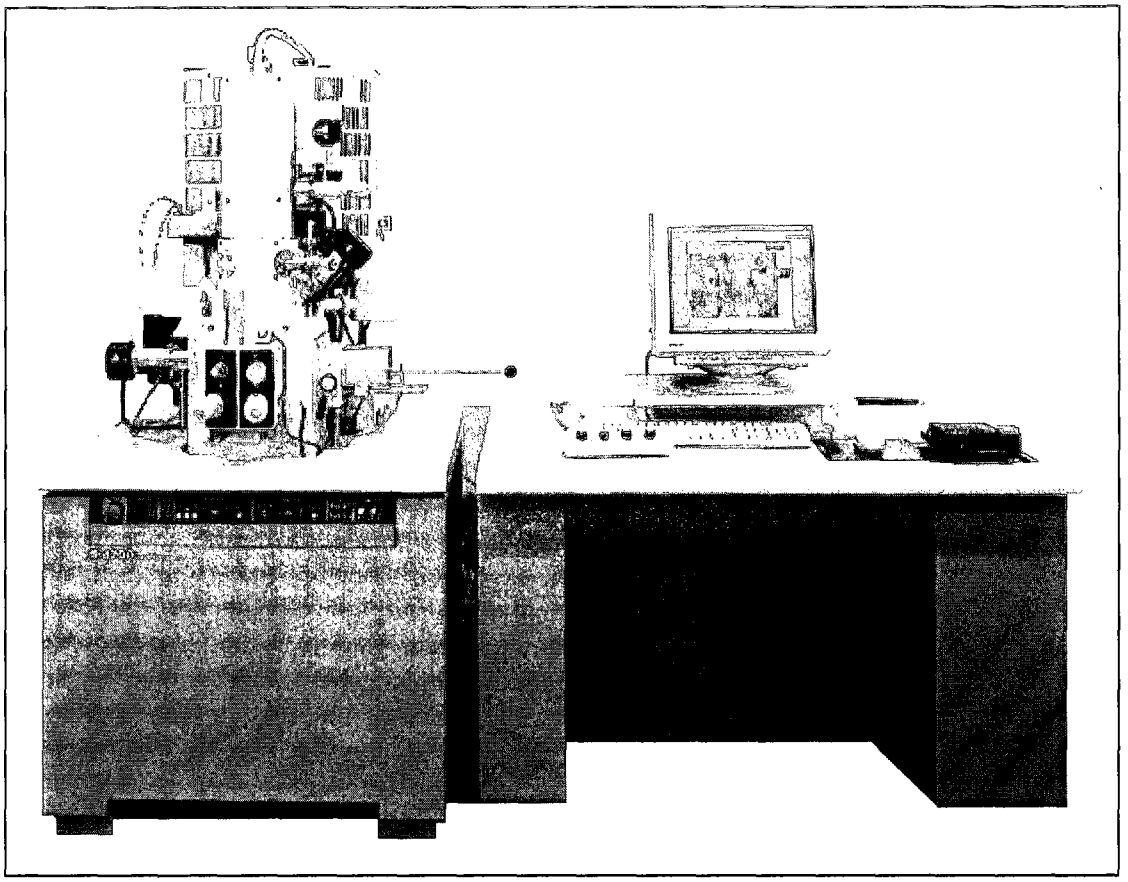

Figure 3.1: Hitachi S-4700 SEM [50]

In a typical SEM, electrons are emitted from a tungsten or lanthanum hexaboride (LaB_6) cathode and are accelerated towards an anode. The electron beam, which typically has an energy ranging from a few hundred of eV to 100 keV, is focused by one or two condenser lenses into a beam with a very fine focal spot sized 0.4 nm to 5 nm. The beam passes through pairs of scanning coils or pairs of deflector plates in the electron optical column which deflects the beam horizontally and vertically so that it scans over an area of the sample surface. When the primary electron beam interacts with the sample, the electrons lose energy by repeated scattering and absorption within a teardrop-shaped volume of the specimen known as the interaction volume, which extends from less than 100 nm to around 5 μm into the surface. The energy exchange

between the electron beam and the sample results in the emission of electrons and electromagnetic radiation; this can be detected to produce an image [49,50].

Many types of samples may be prepared in order to perform SEM analysis. They are the following [49, 50]:

- Metal samples: No special preparation is required other than the ensuring that the specimen is small enough to fit in the specimen chamber.
- Nonconductive solid samples: Should be coated with a layer of conductive material. This prevents the accumulation of static electric fields at the specimen due to the electron irradiation during imaging, and improves the contrast of the image. Coatings such as gold, gold/palladium, platinum, tungsten, graphite etc... have been previously used on samples of this nature.
- Biological samples: A biological specimen requires some kind of fixation in order to preserve its structural properties. This is done by incubating the specimen in a solution such as glutearaldehyde or formalin. Other mechanisms of fixation are cryofixation, cryo-fracture, and freeze-fracture. Cryofixation involves freezing a specimen to liquid helium or liquid nitrogen temperatures at a rate that water forms non-crystalline ice. Cryo-fracture involves fracturing the frozen specimen in a special apparatus. It is then sputter-coated and transferred into a SEM cryo-holder while still frozen. Freeze-fracture is a preparation method particularly useful for examining lipid membranes and their incorporated proteins. This method reveals the structure of proteins embedded in the lipid bilayer.

Gold coating is often a semi-destructive process since removing a gold coating chemically requires aggressive chemicals like potassium cyanide or aqua regia.

SEM spatial resolution is dependant upon the following factors:

- Size of the electron spot which depends on the wavelength of the electrons and magnetic electron-optical system which produces the scanning beam.
- Size of the interaction volume, or the extent to which the material interacts with the electron beam.

SEM has several advantages including the ability to quickly characterize large areas; the ability to image bulk materials (not just thin films or foils). It also offers the variety of analytical modes available for measuring the composition and nature of the specimen [49, 32].

3.2 UV-Vis Spectrophotometry

Spectrophotometry is a technique for the quantitative study of the interaction of a sample with the light. Depending on the wavelength of the light, near-ultraviolet, and visible and near-infrared spectra can be studied. Spectrophotometry involves the use of an instrument called a spectrophotometer, such as that depicted in Figure 3.2. A spectrophotometer measures the intensity as a function of the color, or more specifically, the wavelength of light [51].

Important features of spectrophotometers include the type of light sources, the measurement technique, the spectral bandwidth and the linear range. The most common application of spectrophotometers is the measurement of light absorption, but they can also be designed to measure diffuse or specular reflectance [52]. The use of spectrophotometers is not limited to studies in physics. They are also commonly used in other scientific fields such as chemistry, biochemistry, and molecular biology [51].

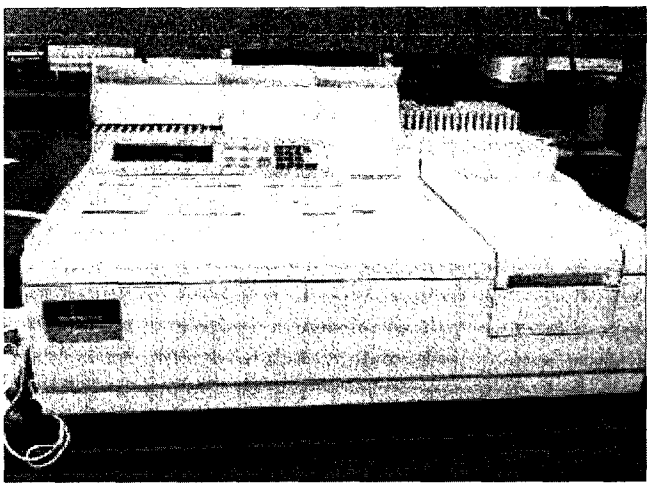

Figure 3.2: Perkin Elmer Lambda 40 UV/VIS Spectrometer

There are two major classes of spectrophotometers:

- single beam
- double beam

A double beam spectrophotometer measures the ratio of the light intensity on two different light paths and a single beam spectrophotometer measures the absolute light intensity. Although ratio measurements are easier, and generally more stable, single beam instruments have some advantages, for instance, they can have a larger dynamic range.

A spectrophotometer consists of the following two parts:

- A spectrometer – produces light of any selected color (wavelength)
- A photometer - measures the intensity of light.

The two components are set up so that a liquid in a cell can be placed between the spectrometer beam and the photometer. The photometer measures the amount of light, which passes through the cell and delivers a voltage signal to a galvanometer. The signal is dependant upon the amount of light, which is absorbed by the liquid [53].

The intensity of color depends upon the concentration of a substance in a solution, which may be measured by determining the extent of absorption of light at the appropriate wavelength. For example, hemoglobin appears red because the hemoglobin absorbs blue and green light rays much more effectively than red. The degree of absorbance of blue or green light is proportional to the concentration of hemoglobin.

For a monochromatic light, there is a quantitative relationship between the intensity of the transmitted light and the concentration of the solution given by equation 3.1 (Beer's law):

$$I = I_0 * 10^{-kcl} \qquad (3.1)$$

- I_0 = Intensity of transmitted light using the pure solvent
- I = Intensity of the light transmitted through the sample
- C = Concentration of the colored compound
- l = Distance the light passes through the solution
- k = Constant.

If the light path l is a constant, as is the case with a spectrophotometer, equation 3.1 may be written in the following manner:

$$I/I_0 = 10^{-kc} = T \qquad (3.2)$$

- k =New constant
- T = Transmittance of the solution

There is a logarithmic relationship between transmittance and the concentration of the colored compound, given by equation 3.3,

$$-\log T = \log 1/T = kc = \text{optical density} = \text{absorbance} \qquad (3.3)$$

The absorbance is directly proportional to the concentration of the colored compound. Spectrophotometry is used not only for colored compounds.

Most organic and inorganic compounds show specific absorption bands due to the fact that the UV-Vis spectra originate from the electronic transitions in molecules. Most spectrophotometers have a scale that reads both in absorbance units, which is a logarithmic scale, and in % transmittance, which is an arithmetic scale [53]

The sequences of events in a spectrophotometer are as follows:

- The light source shines through the sample.
- The sample absorbs light.
- The detector detects how much light the sample has absorbed.
- The detector then converts how much light the sample absorbed into a number.
- The numbers are either plotted, or are transmitted to a computer to be further manipulated (e.g. curve smoothing, baseline correction)

Many spectrophotometers must be calibrated by a procedure known as "zeroing." The absorbency of some standard substance is set as a baseline value, so the absorbencies of all other substances are recorded relative to the initial "zeroed" substance. The spectrophotometer then displays the amount of light absorbed relative to the initial substance [51].

3.3 X-Ray Diffraction (XRD)

X-ray diffraction (XRD) is a powerful non-destructive technique for characterizing crystalline materials. It provides information on structures, phases, preferred crystal orientations (texture) and other structural parameters such as average grain size, crytallinity, strain and crystal defects [54].

X-ray diffraction peaks are produced by constructive interference of monochromatic beam scattered from each set of lattice planes at specific angles. The peak intensities are determined by the atomic deterioration within the lattice planes.

Consequently, the X-ray diffraction pattern is the fingerprint of periodic atomic arrangements in a given material.

A tool used to obtain the characterization of thin film and multilayer structures is Specular X-ray reflectivity X-ray scattering at very small diffraction angles allows characterization of electron density profiles of thin film down to a few tens of angstroms. Using a simulation or the least-squared fit of the reflectivity pattern, one can obtain accurate measurements of thickness, interface roughness and layer density for either crystalline or amorphous thin films or multilayer.

Figure 3.3 depicts the schematic of an XRD system:

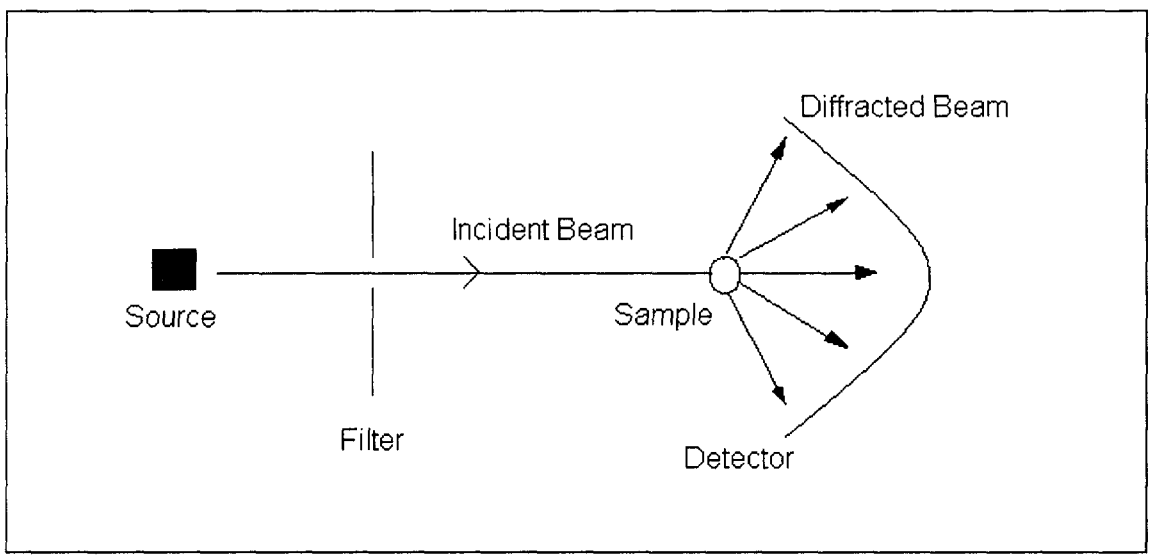

Figure 3.3: XRD System

This method has the following applications:

- Determination of phase contents of reaction products
- Measurements of average crystallite size, strain or micro-strain effects in bulk and thin film samples.
- Quantification of preferred orientation (texture) in thin films and multilayers
- Refinement of lattice parameters

- Determination of thickness, interface roughness and density for thin films and multi-layers

A typical diffractometer consists of a source of radiation, a monochromator to choose the wavelength, slits to adjust the shape of the beam, a sample and a detector. In a more sophisticated apparatus, a goniometer can be used for fine adjustment of the sample and the detector positions. When an area detector is used to monitor the diffracted radiation, a beam stop is usually needed to stop the intense primary beam that has not been diffracted by the sample; otherwise the detector might be damaged. Usually the beam stop can be completely impenetrable to the X-rays or it may be semi-transparent. The use of semi transparent beam stop allows the possibility to determine how much the sample absorbs the radiation using the intensity observed through the beam stop.

3.4 Micro-Raman Spectroscopy

Raman spectroscopy is a spectroscopic technique used in condensed matter physics and chemistry to study vibrational, rotational, and other low-frequency modes in a system. It relies on inelastic scattering, or Raman scattering of monochromatic light, usually from a laser in the visible, near infrared, or near ultraviolet range. The laser light interacts with phonons or other excitations in the system, resulting in the energy of the laser photons being shifted up or down. The shift in energy gives information about the phonon modes in the system. Infrared spectroscopy yields similar, but complementary information [55]

Unlike infrared spectroscopy Raman spectroscopy applied a single frequency of radiation incident on the sample. Here light interacts with molecules, polarizes a cloud of electrons around the nuclei and forms a virtual state or short-lived state. If the incident and scattered light have almost the same frequency or the same energy, it will be called elastic scattering or Rayleigh scattering. In this case the electron is directly

excited from the ground state to the vibrational state. On the other hand, if the nucleus is induced, the energy will transfer from the photon to the molecule or vice versa. In this case, the scattering is inelastic and the photon energy or frequency is changed. This phenomenon is called Raman scattering [56, 57].

To expand further, the Raman effect occurs when light impinges upon a molecule and interacts with the electron cloud of the bonds of that molecule. The incident photon excites one of the electrons into a virtual state. For the spontaneous Raman effect, the molecule will be excited from the ground state to a virtual energy state, and relax into a vibrational excited state, which generates Stokes Raman scattering. If the molecule was already in an elevated vibrational energy state, the Raman scattering is then called anti-Stokes Raman scattering. Figure 3.4 depicts the Rayleigh and Raman scattering phenomenon.

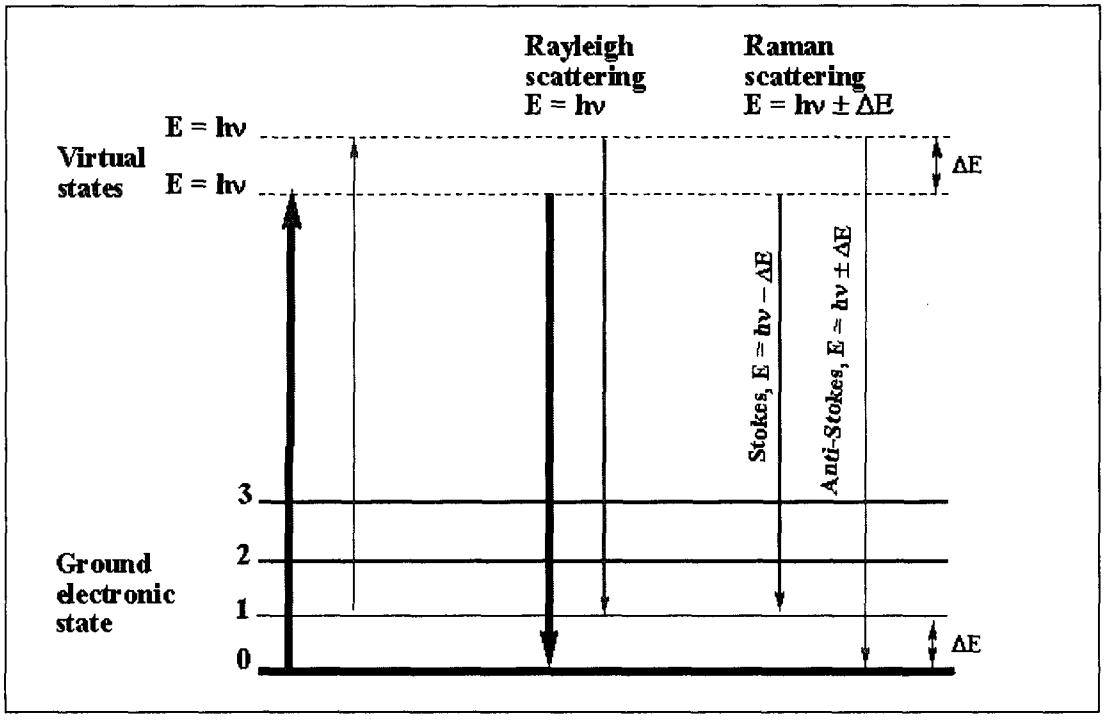

Figure 3.4: Rayleigh and Raman scattering

A molecular polarizability change or amount of deformation of the electron cloud, with respect to the vibrational coordinate is required for the molecule to exhibit the Raman effect. The amount of the polarizability change will determine the Raman scattering intensity, whereas the Raman shift is equal to the vibrational level that is involved [55].

Several variations of Raman spectroscopy have been developed, they are the following:

- surface-enhanced Raman- to enhance the sensitivity
- Raman microscopy - to improve the spatial resolution
- Resonance Raman - To acquire very specific information

In this research Surface Enhanced Raman Spectroscopy (SERS) was of particular interest. SERS may occur in a silver or gold colloid or a substrate containing silver or gold. Surface plasmons of silver and gold are excited by the laser, resulting in an increase in the electric fields surrounding the metal. Given that Raman intensities are proportional to the electric field, there is large increase in the measured signal (by up to 10^{11}). This effect was originally observed by Fleishman but the prevailing explanation was proposed by Van Duyne in 1977 [55].

There are several advantages of the micro-Raman technique when studying solids, they are the following:

- The method is contactless and therefore allows non destructive microanalysis of structural properties.
- No sample preparation is required, which is a crucial point when characterizing processed devices.
- The high spatial resolution obtained with the Raman microscope is another fundamental benefit that allows to probe smaller dimensional scale devices.

This is important for the analysis of microstructures and devices, where the properties of the layers are strongly process dependent and may differ significantly from the bulk material properties. Micro-Raman system is one of the preferred methods when characterizing semiconducting materials and thin films.

In our research the apparatus used to record the Raman spectra was a Labran high resolution (HR) with a Raman-IR micro analytical spectrometer equipped with following:

1) A 17 mW He-Ne laser emitting at 632.8 nm
2) A holographic notch filter (Kaiser Optical System, Model:Super Notch-Plus)
3) A 256 x 1024 – pixel CCD detector
4) A computer-controlled XY stage with a spatial reolutin of 0.1 μm
5) Two interchangeable gratings (950 and 1800 mm -1, respectively)
6) A confocal microscope with 10, 50, 100 x objectives with a lateral spatial resolution of approximately 10, 2 and 1 μm, respectively

The laser power was 9 mW on the sample surface and the spectral resolution is less than 0.5 cm -1 for a slit width of 150 μm and a confocal hole of 300 μm. Micrometric imaging has been performed, two samples areas of respectively 25 x 25 μm and 10 x 10 μm were considered and the laser beam is scanned over it by moving the sample with the computer-controlled XY stage. Finally the divisions of the total area in cells of 3x3 μm and 1x1 μm have been chosen.

The micro-Raman analysis was performed with a high resolution (HR) combined Raman-IR micro analytical apparatus, equipped with a motorized xy stage and auto focus. The spectra were generated with 632.8 nm He-Ne laser excitation. The power of the laser out of the objective, a 100 x with numerical aperture (NA) of 0.90, was about 9mW, and the focused laser spot had a 1 micrometer diameter. The spectral resolution of this apparatus is estimated to be around 0.5 cm-1 for a slit width of 150 μm and a

confocal hole of 300 μm. Two different acquisition modes were used. The first was the single point acquisition while tin the second acquisition mode, an area is defined on the sample and the laser beam is scanned over it by moving the sample with the computer-controlled XY stage. In this study, a division of the total area in cells has been chosen. The apparatus used during this study is depicted below in figure 3.5.

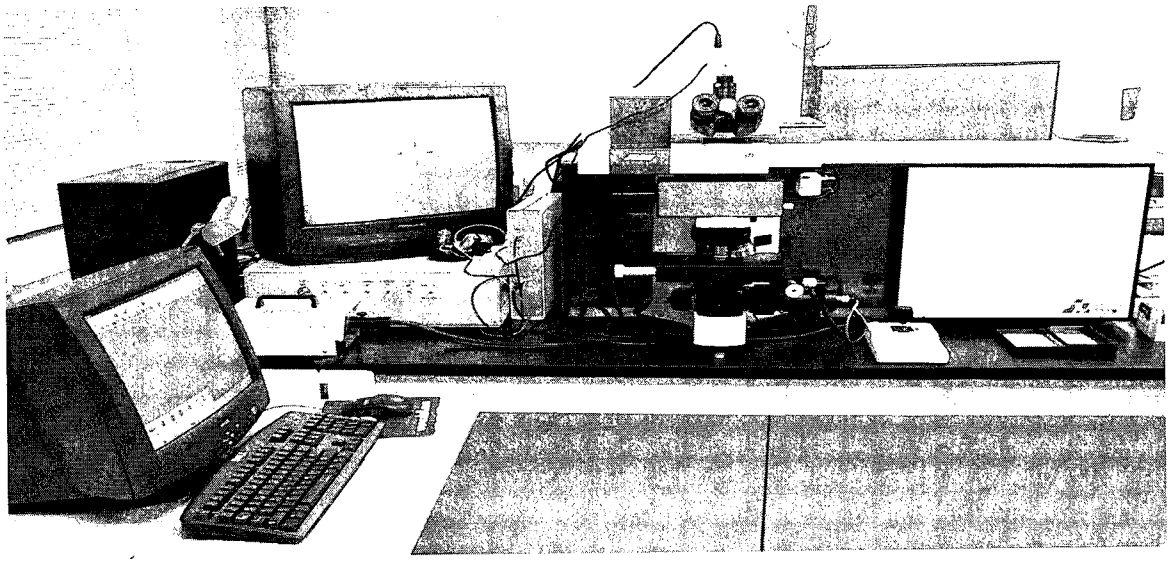

Figure 3.5: Labran HR with Raman-IR microanalytical spectrometer

Chapter 4 : Sample Preparation

Many samples were prepared for the purpose of this research. The substrates were cleaned and silanized, after which gold nanohole and nanoring structures were fabricated by using a modified nanosphere lithography technique. Once this was completed the substrates were functionalized, in order to study the biomolecular interactions with fibrinogen, amyloid β–derived diffusible ligands (ADDL), and protein (AT5G07010.1) and its respective antibody.

4.1 Substrate Preparation

Rectangular glass substrates, which measured 7 cm in length, 8 mm in width, and 1mm in thickness were used. The glass substrates were cleaned using the following procedure:

1) Glass slides were washed with soap and copious amounts of water
2) Following this step they were washed with de-ionized water and acetone
3) Once washed the substrates were laid out to dry
4) The substrates are then washed with isopropanol, to remove acetone from the substrates
5) The substrates were once again laid out to dry
6) Following this step, the substrate was immersed in a solution of (3-aminopropyl) tris [2-(2methyloxyethoxy)] silane in acetone (2%) for 15 minutes.
7) The substrate was then washed once again with acetone and isopropanol and used immediately.

The clean glass substrates were activated by silanization as described in step 6 due to the fact that it facilitates the subsequent absorption of the gold colloids onto the

glass substrate. The silane molecule has an amino (NH2) group at one end as depicted in figure 4.1. The gold nanoparticles will bind to silane, through the lone pair of the nitrogen atom and, therefore, adhere to the glass substrate. Furthermore, the silicon atom forms a covalent bond with the OH (hydroxyl) groups adsorbed on glass.

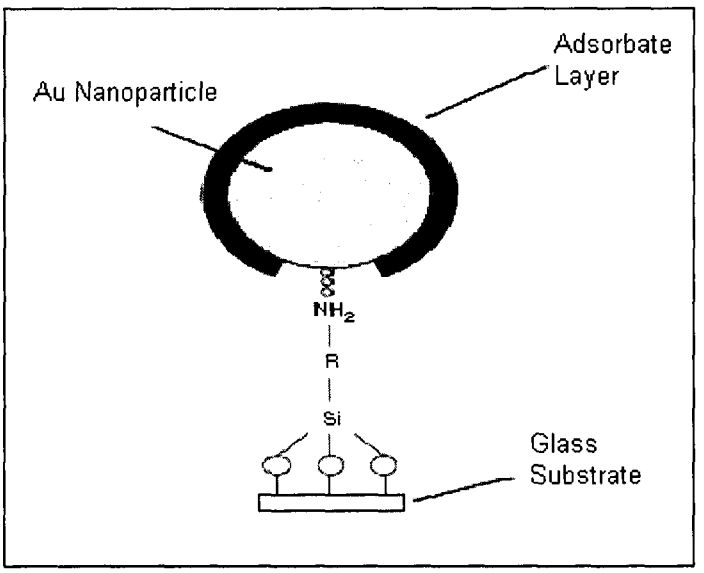

Figure 4.1: Au stabilized with COO- groups (adsorbate layer) attached to the silanized glass [58]

4.2 Gold and Polystyrene Composite Preparation by Self Assembly

Gold colloids were prepared by sodium citrate reduction of chloroauric ($HAuCl_4.3H2O$) according to Turkevich's method [59]. The procedure was the following:

1) Sodium citrate solution was prepared (1% solution in DI water)
2) 15-20 mg of chloroauric acid was dissolved in ~80mL of DI water
3) The solution was heated
4) Once the solution began to boil, 5 mL of the sodium citrate solution was added to the mixture, which resulted in a blue hue

5) The solution was boiled for another 10-15 minutes and then left to cool down to room temperature. Once ready the solution became a deep red/purple, the colour corresponding to the colloidal gold formed.
6) This resulted in Gold (III) chloride hydrate – gold colloids approximately 20 nm in diameter

The gold colloids were added to a suspension of polystyrene microspheres in water; the spheres having an average diameter of 100, 200, 520 and 750 nm. The substrate was immersed in a glass vial containing the mixture of PS microspheres and Au colloids; the gold-PS composite structure is fabricated by self-assembly on the cleaned, silanized glass substrate. For an increased absorption of the gold colloids onto the glass substrate, the glass was activated by silanization as mentioned in the previous section. As depicted in figure 4.1, the nanoparticle is shown in grey; the black part shows the citrate groups adsorbed on the gold (citrate comes from the synthesis of gold and has carboxyl groups); the carboxyl groups have a negative charge which helps to stabilize the gold (by repulsion). The substrates were kept in this mixture at 55-60°C for 2-3 days, until the whole amount of suspension was deposited; multilayers of ordered PS-Au structures were formed on the glass substrate. The composite samples were then annealed by keeping them at a temperature slightly above the glass transition temperature of PS. During the annealing process the Au nanoparticles move and form a ring-structure around the PS microspheres. Following this, the Au-PS composite films were immersed in anhydrous ethanol and agitated in an ultrasonic bath, to remove the PS spheres. Once PS is dissolved in ethanol the Au nanoparticles will form a ring around the holes during annealing left behind by the dissolution of PS. Raman and SEM studies have shown that a part of PS cannot be removed even after prolonged times of stirring in ethanol, as they "stick" to the substrate. Multiple batches of samples were prepared; they have been detailed in table 4.1 below.

Batch	Name of the Sample	Size of Polystyrene (PS) (nm)	Composition	Annealing Conditions		Comments
				Temperature °C	Time (min)	
I	5	530	2 drops PS + 1 mL Au	92	10	Used Commercial Gold for Batch 1 Diamter of Au: 20 nm
	6	530	2 drops PS + 0.5 mL Au	90	20	
	7	530	2 drops PS + 0.5 mL Au	90	30	
	8	530	2 drops PS + 0.5 mL Au	90	50	
II	2A	200	2 drops PS + 0.5 mL Au + 1 mL H_2O	82	20	Used Gold prepared in lab for Batch 2 Diameter of Au: ~12 nm
	2B	200	2 drops PS + 0.5 mL Au + 1 mL H_2O	72	30	
	2C	200	2 drops PS + 0.5 mL Au + 1 mL H_2O	64	30	
	5A	500	2 drops PS + 0.5 mL Au + 1 mL H_2O	82	20	
	5B	500	2 drops PS + 0.5 mL Au + 1 mL H_2O	72	30	
	5C	500	2 drops PS + 0.5 mL Au + 1 mL H_2O	64	30	
III	1A	100	2 drops PS + 1 mL Au + 0.5 mL H_2O	105-110	30	Used Gold prepared in lab for Batch 2 Diameter of Au: ~12 nm Sample 1A', 2A', 7A' not annealed
	1A'	100	2 drops PS + 1 mL Au + 0.5 mL H_2O	-	-	
	2A	200	2 drops PS + 1 mL Au + 0.5 mL H_2O	105-110	30	
	2A'	200	2 drops PS + 1 mL Au + 0.5 mL H_2O	-	no	
	7A	700	2 drops PS + 1 mL Au + 0.5 mL H_2O	105-110	30	
	7A'	700	2 drops PS + 1 mL Au + 0.5 mL H_2O	-	-	
IV	2A	200	2 drops PS + 1.5 mL Au	90-95	70	Used Prepared Gold for Batch 2 - ~12 nm Sample 7A' not annealed
	2B	200	2 drops PS + 1.5 mL Au	90-95	70	
	5A	500	2 drops PS + 1.5 mL Au	90-95	70	
	5B	500	2 drops PS + 1.5 mL Au	90-95	70	
	7A	700	2 drops PS + 1.5 mL Au	90-95	70	
	7B	700	2 drops PS + 1.5 mL Au	90-95	70	
	7B'	700	2 drops PS + 1.5 mL Au	-	-	

Table 4.1: Parameters used for Platform Preparation

4.3 Functionalization

The Au film was functionalized with 3-mercaptopropionic acid (MPA) by immersing it for 30 minutes in a 10 mM solution of MPA in absolute ethanol. The Au MPA sample was then immersed in a carbodiimide solution in ethanol for 10 minutes. 3-Mercaptopropionic acid has an **S-H (thiol)** group which has a high affinity towards gold (Figure 4.2). It forms a covalent S-Au bond and the acid molecules will align on the gold surface. They form a Self-Assembled Monolayer (SAM) on the gold surface having the carboxyl groups oriented toward the biomolecule. SAM is used in almost all sensor applications to help to attach the biomolecules to the Au surface.

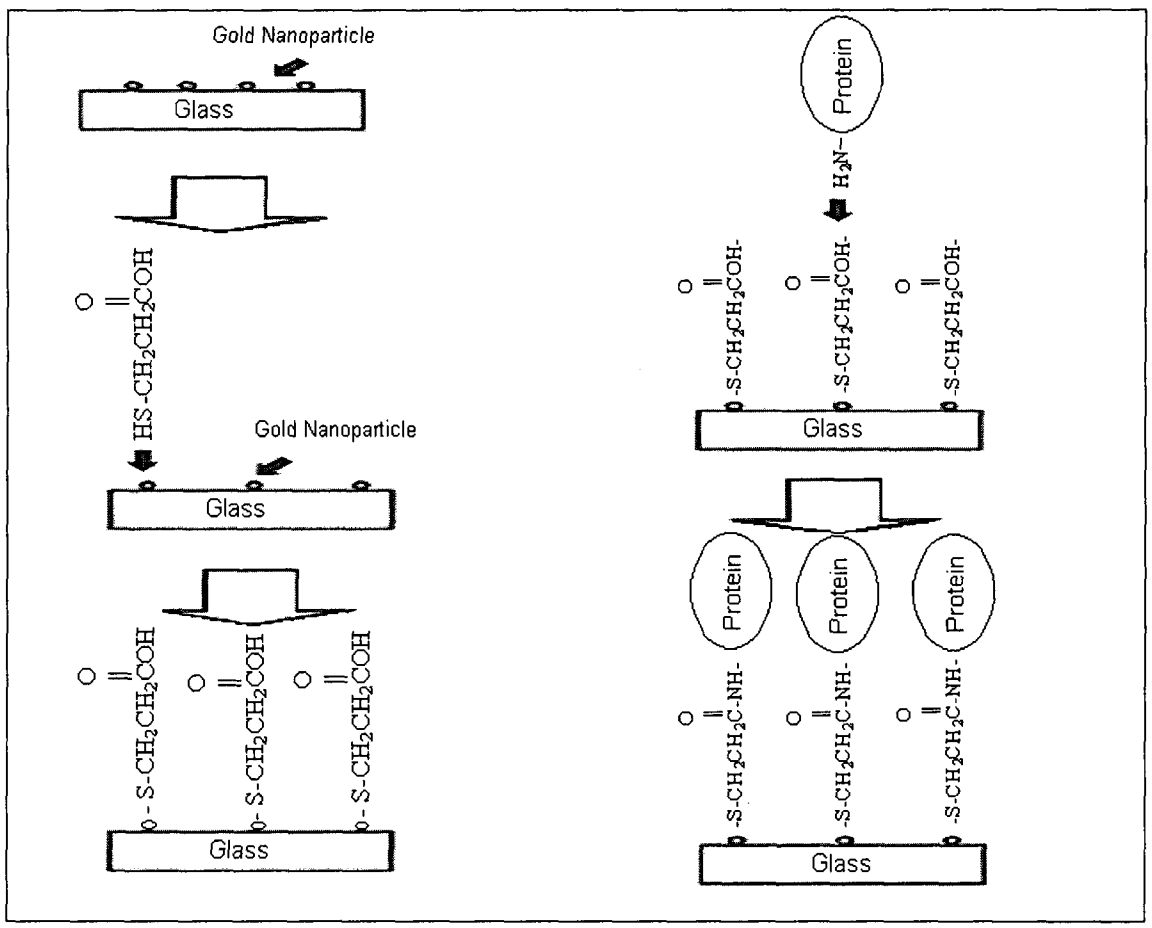

Figure 4.2: Functionalization of Au nanoparticles with 3-mercaptopropionic acid

SAM may be described in general by figure 4.3. SAMs are formed by simply immersing a substrate into a solution of the surface-active material, in our case the SAM is adsorbed on gold. The formation of the 2D assembly includes chemical bond formation of molecules with the surface and with an e.g. biomolecule in our case. It should be noted that between gold and the end group there are alkyl (CH_2) goups. We have used 3-MPA to functionalize Au nanoparticles in order to facilitate the biomolecule attachment.

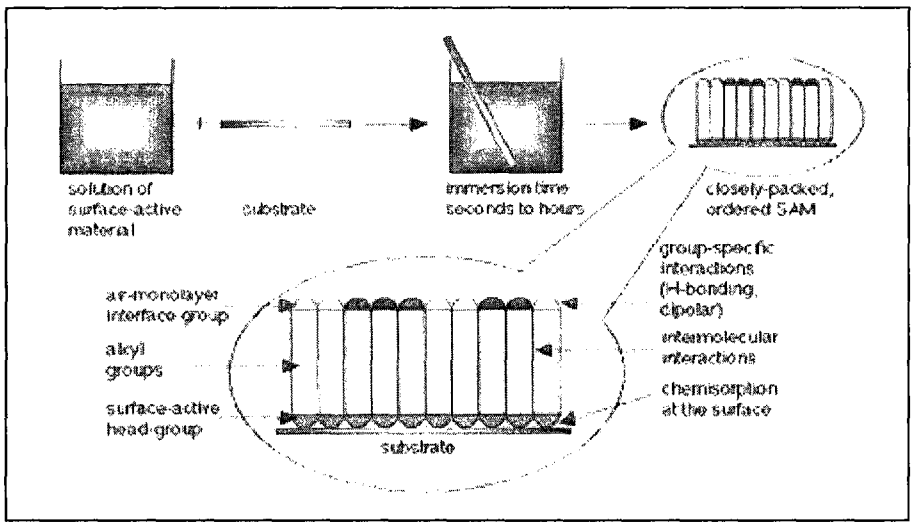

Figure 4.3: Self Assembled Monolayer [60]

4.4 Preparation and Purification of Biomolecules

The following biomolecules were used during the course of this research:

- Fibrinogen
- amyloid β–derived diffusible ligands (ADDL)
- Protein (AT5G07010.1) and its respective antibody

Fibrinogen was purchased from Sigma Aldrich, and was used as is. ADDL was prepared from the polypeptide Amyloid β 1-42 (A β 1-42) according to Lambert's procedure [61], and deposited on the functionalized substrate. The protein,

AT5G07010.1 was prepared as detailed in the QIAexpressionist [62], and deposited along with its antibody on the substrates.

4.4.1 ADDL Preparation

ADDL as stated above was prepared using the Lambert procedure [61]. There are two parts to the procedure; the first part details the Monomerization (polymer that defragments into monomers) by HFIP and storage of Aβ peptide, the second part details the ADDL preparation.

The solid Aβ peptide (1–42) was stored as a solid at −80 ◦C. Once we were ready to prepare the stock peptide films, the Aβ peptide was placed on ice. Following this the 1,1,1,3,3,3-hexafluoro-2-propanol (HFIP which is highly corrosive and very volatile, Sigma H-8508) was placed on ice in the hood and allowed to cool. A sufficient amount of HFIP was added to the solid Aβ peptide such that the final peptide concentration was 1mM (e.g. 2.217 ml cold HFIP). The vial was then thoroughly rinsed. The mixture was then incubated at room temperature for 60 minutes; at all times the vial was kept closed, and it was observed that the solution was clear and colorless as described in the original procedure. If the solution had turned yellow in color or any cloudy suspension was observed, this would have implied poor peptide quality, and the solution would have been discarded. The peptide-HFIP solution was placed back on ice for 5-10 minutes. The solution was aliquoted into non-siliconized microcentrifuge tubes (e.g. (e.g. 100 [1]l = 0.45 mg for Aβ 1–42) while keeping the tube covers open. HFIP was evaporated overnight under the hood at room temperature. Following this the tubes were transferred to a speedvac, and dried down for 10 minutes; the objective of this was to ensure that all traces of HFIP were removed. The resulting peptide, was a thin clear film at the bottom of the tubes; the peptide was not white or chunky indicating that the

peptide was prepared in an appropriate manner. The peptide films were then stored over desiccant at −80 ◦C.

Following the monomerization procedure ADDL was then prepared. The peptide film as detailed above was removed from the −80 ◦C freezer and placed on ice. A 5mM Aβ stock in 100% DMSO was prepared by adding 20 µl fresh anhydrous DMSO (Sigma Hybri-Max D-2650) to 0.45 mg peptide. The sides of the tube were thoroughly washed in order to ensure the resuspension of the peptide film (DMSO stock was clear in color, and since DMSO is very hygroscopc, fresh ampoules were used for each preparation. 5mM peptide stock into F12 medium without phenol red (BioSource Inc., custom preparation) was diluted. A volume of 5mM peptide stocks were then freshly prepared; according to Lambert yield, the ADDL solution should be no greater than 100 µM (e.g. 20 µl DMSO stock to 980 µl F12). This was then incubated at 5 °C for 24 h, and centrifuged at 14,000 × g for 10 min in the cold. The supernatant was then transferred to a new tube. This supernatant was ADDL [61].

4.4.2 Protein and Antibody Deposition

AT5G07010.1 is a protein found in Arabidopsis; a small flowering plant related to cabbage and mustard. It is one of the model organisms used for studying plant biology and the first plant to have its entire genome sequenced. AT5G07010.1 has a molecular weight of 41364.0 Daltons.

The preparation of the antibody, and the protein was completed by biological experts, and the detailed procedure has been provided in Appendix A [63, 64].

The procedure in order to bind the antibody to the substrate is the following:

- Take the Polyclonal antibody 1:1000 Dilution in PBS + 1% (w/v) BSA → equivalent to taking 10 mL of the buffer + 10 µL of the antibody + 1% of the BSA
- Hybridization = 1 hour incubation

- Wash 3 times in PBS + 0.05% Tween 20 → e.g. 50 µL/100mL
- Measure

The procedure in order to bind the Protein to the substrate is the following:

- Bind the antigen AT5G07010.1
- Bind protein BSA or defated milk → 3% (w/v)
- Incubate 1 hour
- Wash 3 times in PBS + 0.05% Tween 20
- Measure

It should be noted that washing = 5 minutes and incubation = 1 hour.

BSA was used to block unoccupied sites after the initial adsorption of antibodies to avoid nonspecific adsorption of the antigen. This means that the antigen would only be adsorbed on the antibody and not on gold as all the sites are occupied by BSA.

It should be noted that the composition of PBS, phosphate buffered saline, is the following:

- 0.15M NaCl
- 82% vol 0.01% M Na_2HPO_4
- 18% vol 0.01 M KH_2PO_4
- pH set to 7.4 using a pH-meter with NaOH/HCl at room temperature

Chapter 5 : Results and Discussion

5.1 Structure and Morphology of the Gold Nanostructures

5.1.1 Structure of the Gold Nanoparticles

Figure 5.1 depicts wide-angle X-ray diffraction patterns of multilayer samples of PS-Au composites. These samples were prepared by vertical deposition method with two different gold-polystyrene ratios (trace a and b respectively). Vertical deposition refers to the preparation of the sample at a particular angle and rate of deposition. Trace a corresponds to the sample prepared with 80μg/mL Au: 1 mL aqueous suspension of PS (5%w/v). Trace b corresponds to the sample prepared with 200μg/mL Au: 1 mL aqueous suspension of PS (5%w/v). Trace c corresponds to a composite sample with an amount of gold that is too low to be detected; therefore there are no reported peaks. The last trace is a reference trace corresponding to the glass substrate.

Broad peaks at low angles, marked by dashed vertical lines, are typical of bulk atactic (not an ordered polymer) polystyrene. In trace b, the (111) and (200) diffraction lines of the fcc colloidal gold particles can be distinguished (see the reference for fcc Au at the bottom of Figure 5.1). Their line-widths indicate particle sizes of about 9 and 6 nm for the <111> and <200> directions respectively. In trace a only a weak (111) peak is present. X-ray scattering of a monolayer sample produced by vertical deposition, trace c, does not differ significantly from the scattering of an empty glass slide [65].

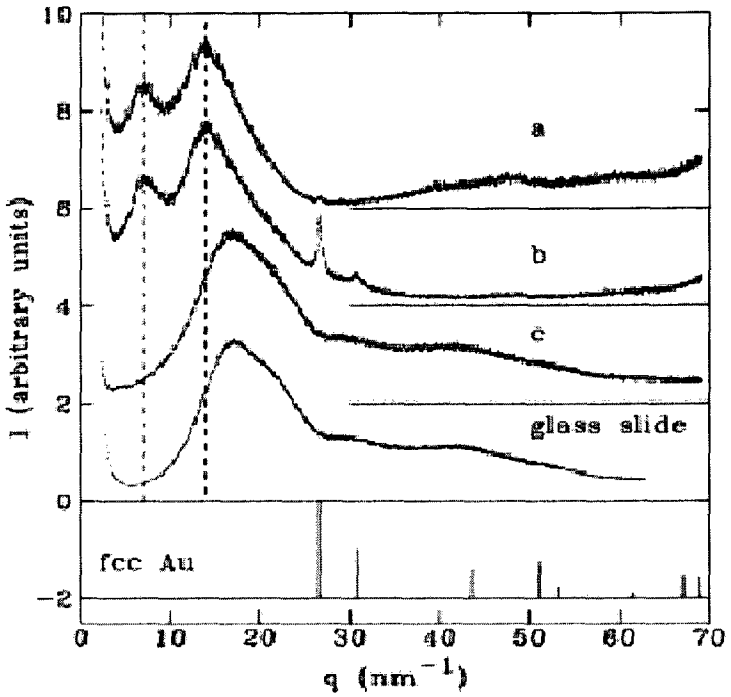

Figure 5.1: XRD pattern of Au-PS composites prepared by vertical deposition method [65]

5.1.2 Morphology of Gold Nanostructures

Multiple samples were prepared in order to study the morphology of the gold nanostructures prepared through the procedure described in Chapter 4. The conditions under which the samples were prepared are given in table 4.1. SEM images of the samples revealed the presence of arrays of sub-wavelength holes, and some samples depicted the presence of both holes and rings.

Figure 5.2 is an AFM image of the Au-PS colloidal crystal (Au cannot be seen) showing the highly ordered structure. The two areas indicated in the image correspond to the two crystalline forms. It can be seen that there are multilayers of composites. In this particular case, they were 18-20 layers [65].

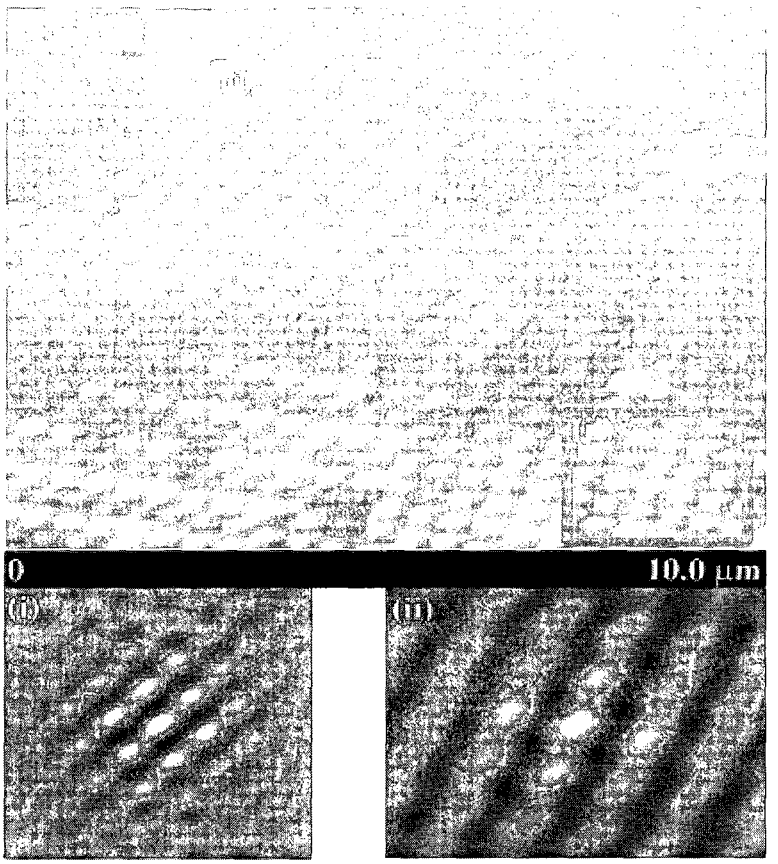

Figure 5.2: PS microspheres: 510 nm; Au: 5 nm Vertical deposition 55°C, 3 days – both i) hexagonal and ii) tetragonal structures were observed [65]

Figure 5.3 shows the SEM image of a sample prepared with 700 nm PS spheres which was not annealed. The image confirms the presence of both structures, i.e. nanorings, and nanoholes; in our case the ring structure is not a continuous ring structure rather it is a ring made up of nanoparticles, which do not touch one another. It is believed, based on our experimental data, that heating the sample would increase the number of ring structures due to the migration of gold particles. In the non-annealed samples the nanohole structures prevail. The sensitivity is determined by the size of the holes in both annealed and non-annealed samples. This will be further discussed in the upcoming sections.

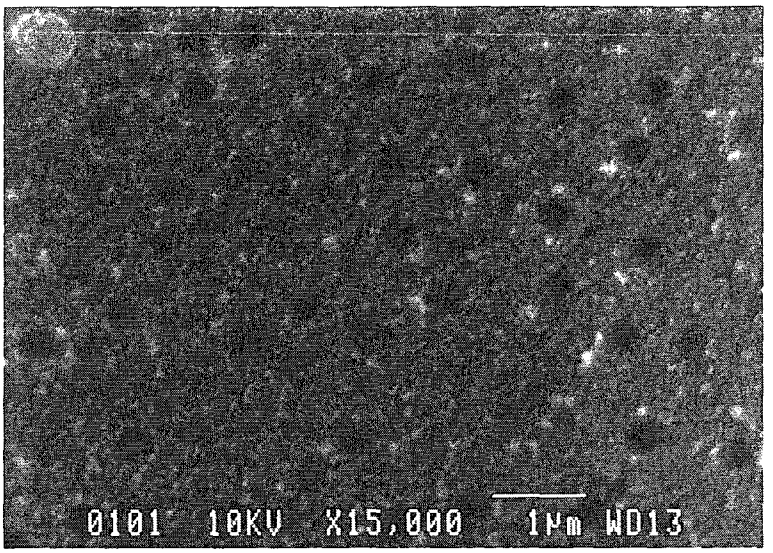

Figure 5.3: SEM image of an unannealed sample showing both nanoring and nanohole structures

Figure 5.4 is an SEM of another sample at a higher magnification, prepared with 700 nm PS spheres which was not annealed. This image contains nanorings, and some aggregation effects can be observed around the holes. The structures are well defined; however they are not evenly distributed when compared to the previous images. It can be observed that in the left corner of the image, the spheres are not completely removed. Furthermore, since larger spheres were used in order to prepare these samples, there are fewer binding sites, which reduces' the sensitivity of the sensor. The figure also shows the presence of gold nanoparticles and aggregates, uniformly distributed between the holes. This is similar to the inset presented in the figure 5.8.

Figure 5.4: SEM image of a nanohole and nanoring structure prepared with 700 nm PS (no annealing)

Figure 5.5 is an SEM of a sample prepared with 100 nm PS spheres which was not annealed. This image shows only ring structures, however not very well defined. Despite the fact that the structures are not very well defined, the sensitivity of this platform proved to be very high. The reason for this is due to the elevated number binding sites for the biomolecules; in the case of larger spheres, there are fewer binding sites.

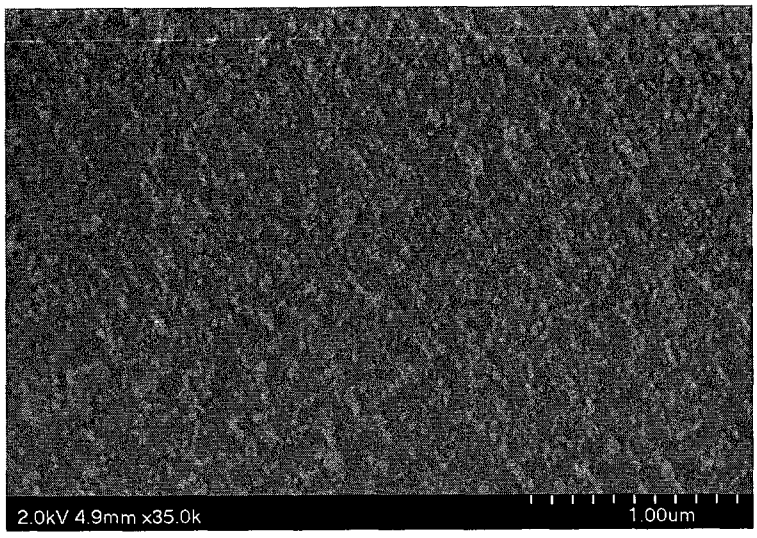

Figure 5.5: SEM image of an unannealed sample showing nanoring structures - 100 nm spheres

Figure 5.6 is an SEM of a sample prepared with 200 nm PS spheres which was not annealed. This image shows nanohole structures over a larger area. It can be seen from this image that the structures are quite evenly distributed. Furthermore, it may be observed that the number of holes i.e. number of binding sites is quite dense. As mentioned above, the sensitivity of this platform proved to be quite high, due to the elevated number of binding sites.

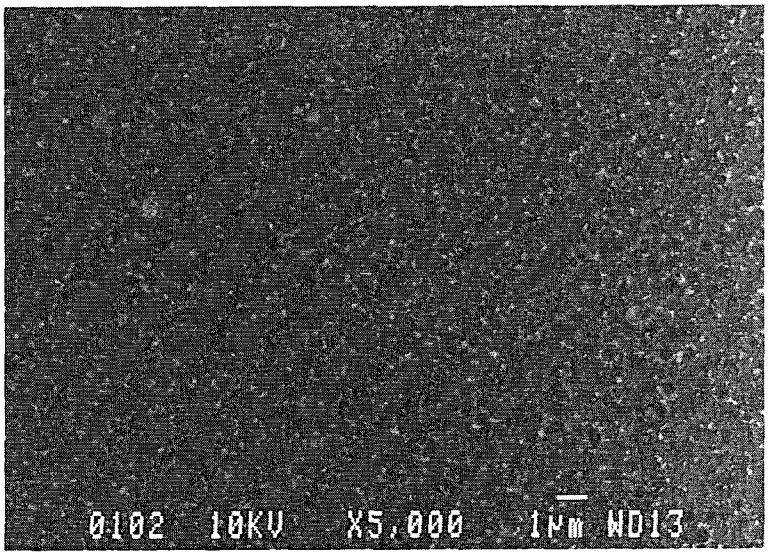

Figure 5.6: SEM image of a nanohole structure prepared with 200 nm PS (no annealing)

Figure 5.7 is an SEM of another sample prepared with 200 nm PS spheres which was not annealed. In this sample the holes are better defined and the structure is more ordered when compared to the sample fabricated with very small spheres i.e. 100 nm. In the middle of this image it was observed that there are some structures which were not perfect. Both the size of the holes and the quality of the structure influence the sensitivity of the platform. It should be noted that there are some small differences between samples prepared under identical conditions. In this case, Figure 5.6 and Figure 5.7 portray two samples prepared in the same manner however the SEM images are not identical. This may be attributed to the quality (size distribution) of the gold structures that were used during the synthesis.

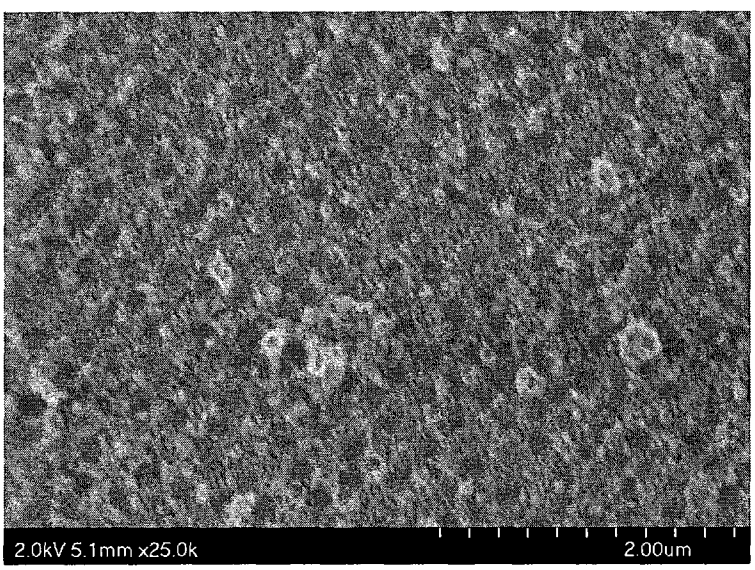

Figure 5.7: SEM image of a nanohole structure prepared with 200 nm PS (no annealing)

Figure 5.8 shows the SEM image of an array of sub-wavelength holes surrounded by rings formed by Au nanoparticles. The array shown in the image was fabricated with 530 nm PS microspheres and 20 nm commercial gold colloids, and annealed at 90°C for 20 min. The hole density as calculated from the image was found to be 3.3/μm^2. The diameter of the holes was found to be 297 nm and the center-to-

center distance 559 nm (average value). The figure shows the presence of gold nanoparticles and aggregates, uniformly distributed between the holes.

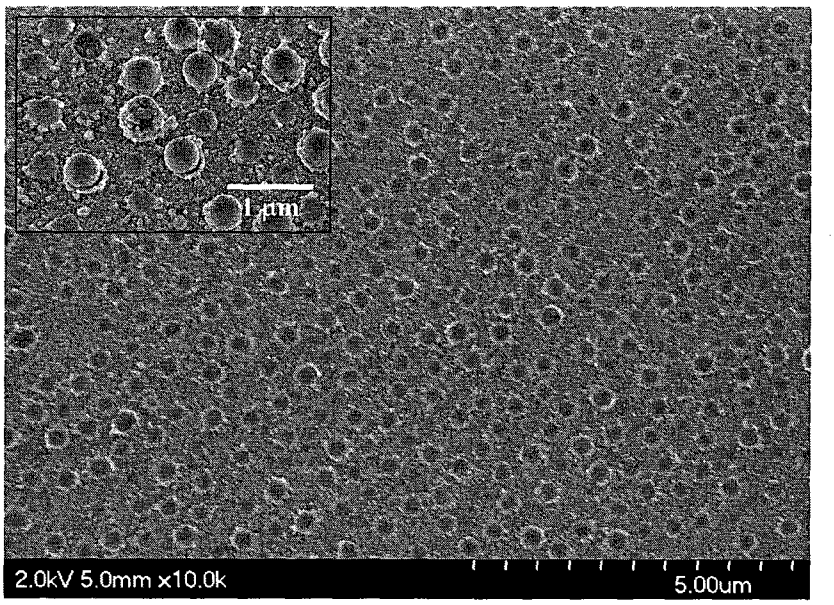

Figure 5.8: SEM image of a nanohole/nanoring array - Inset: Enlarged image of a region where PS spheres were not completely removed.

In order to understand the hole structure formation mechanism, we have studied the image in an area where the PS microspheres were not yet completely removed (Figure 5.8 inset). The figure clearly shows the ring structures around the base of the spheres and around the holes in the places where PS spheres were already removed. It can be seen that some of the spheres are almost completely covered by Au nanoparticles which, during the dissolution would fall and reinforce the rings. The Au nanoparticles on top of the spheres originate from the superior layers.

5.1.3 Geometrical Characteristics

The parameters that define the nanohole structures are the following:

- the diameter of the holes
- the spacing of the holes

- the density of the holes

Figure 5.9 – 5.12 shows the dependencies of the geometrical characteristics calculated from the SEM images of the gold nanostructures on the size of the PS microspheres.

In Figure 5.9 it can be seen that the average spacing of the holes increases linearly with the diameter of the PS spheres. This implies that smaller spheres lie closer together and larger spheres are spaced further apart, which is visible in the images, and from calculations.

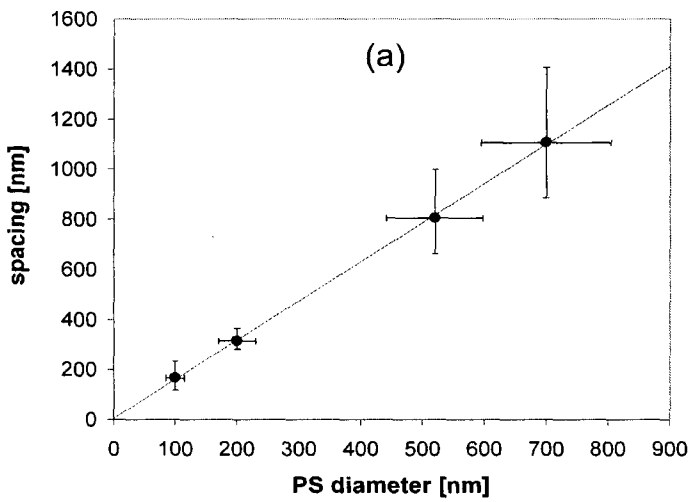

Figure 5.9: Polystyrene diameter vs spacing

In Figure 5.10, it can be seen that the average hole diameter increases linearly with the diameter of the PS spheres. The footprints of larger spheres result in larger holes; this implies that larger spheres result in larger holes.

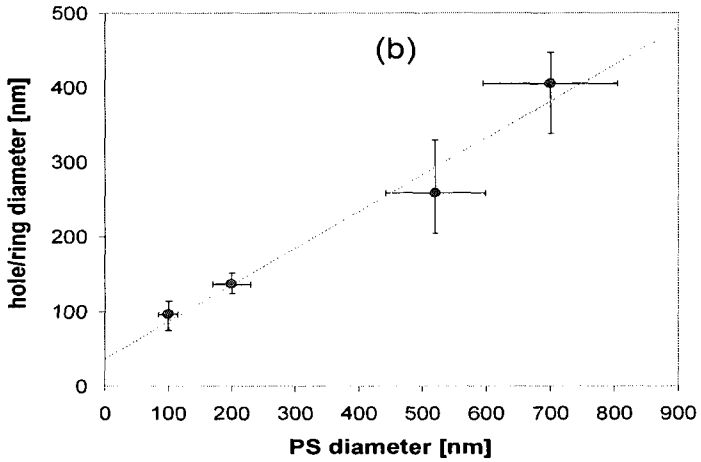

Figure 5.10: Polystyrene diameter vs hole/ring diameter

Figure 5.11 depicts that the density of the holes (number of holes/μm2) decreases as the sphere sizes increases.

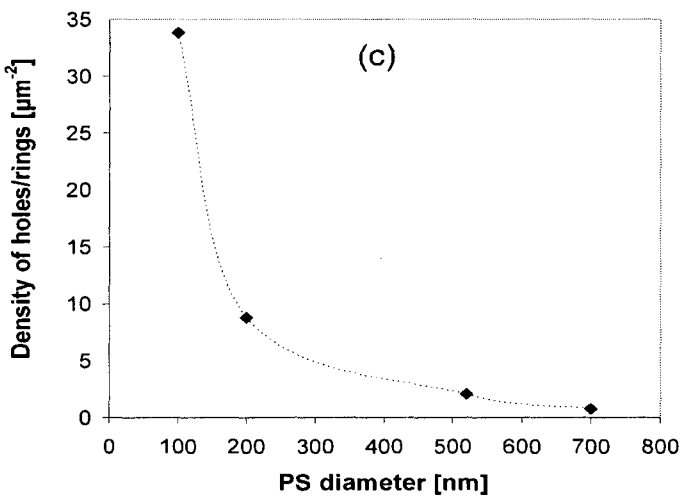

Figure 5.11: Polystyrene diameter vs Density of holes/rings

Figure 5.12 confirms the direct relationship between the geometrical characteristics of the Au nanostructures and their sensing capacity. The figure clearly shows that the sensitivity of the structure (Sensitvity (S) = $\Delta\lambda/\Delta n$ – see section 5.2) actually decreases with the average spacing between the spheres, and that it is higher

for the spheres with a smaller diameter. Therefore smaller spheres result in more sensitive devices.

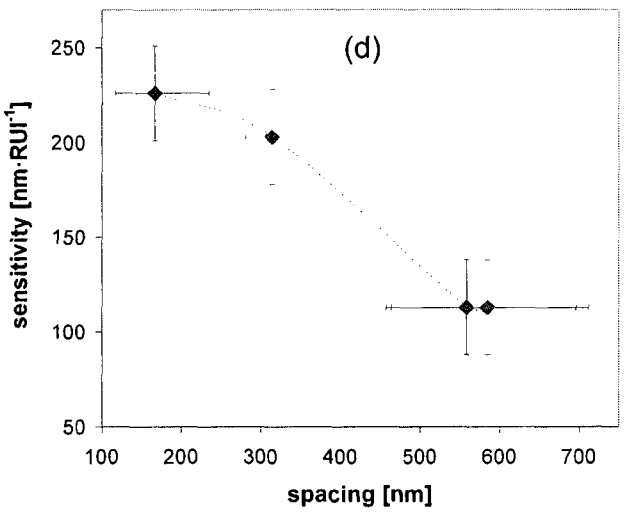

Figure 5.12: Spacing vs Sensitivity

The relationships shown in Figure 5.9 – 5.12 are in agreement with the mechanism of the formation of the hole arrays. Indeed, when the multilayer structure collapses during the dissolution of the spheres, the only layer that remains is the first one containing the gold nanoparticles directly absorbed on the glass substrate.

In summary, the graphs present very important results concerning the influence of the geometrical characteristics on the sensitivity of the platform. The size of the PS spheres used to prepare the composite determines the spacing between the holes, the diameter of the hole/ring and their density, i.e. the number of holes/rings per square microns. Furthermore, sensitivity is highest for the smallest spheres.

5.2 Sensitivity of Sensor Platforms

In order to calculate the sensitivity of the structures, the spectrum was measured for each sample. The absorbance spectra of the samples were recorded in the visible region, in water, acetone and 2-propanol environments. The position of the gold SPR

band and its absorbance were monitored for each case. Table 5.2 lists the characteristics of the gold SPR band of different platforms in water and in an acetone environment.

Batch	Name of the Sample	T °C	λ nm (H_2O)	A (H_2O)	λ nm (Ac)	Δλ nm (Ac)	A (Ac)	S nm/RIU (Ac)
I	C AU	90	530	0.22	535	5	0.2	195
II	2A	82	545	0.32	550	5	0.37	195
	2B	72						
	5A	82	540	0.47	545	7	0.37	273
III	1A	105	550	0.41	552	2	0.57	78
	1A'	-	540	0.77	550	10	0.53	391
	2A	105	555	0.24	560	5	0.65	195
	2A'	-	555	0.3	562	9	0.37	352
	7A	105	550	0.66	560	10	0.68	391
IV	2A	90	542	0.72	550	8	0.68	313
	2B	90	540	0.77	550	10	0.72	391
	5A	90						
	5B	90	538	1.6				
	7A	90	550	0.9				

Table 5.1: Characteristics of Gold SPR band in Water and Acetone

The samples listed in table 5.1 were prepared under different conditions, and different temperatures. The annealing temperatures are indicated for all samples; for samples 1A', 2A' there was no annealing. In order to calculate the sensitivity of the different sensor platforms, their UV-Vis spectra and absorbance (A) representing the intensity of the band were measured, following this the position of the SPR band was found and used to calculate the sensitivity (λ). The shift of the SPR band (Δλ) is calculated in a solvent (in this case acetone) compared to water. Δλ was calculated by subtracting λ in acetone from λ obtained in water. The change in the refractive index

was 0.0256 ($n_{acetone}$ = 1.3586 - n_{water} = 1.333). Sensitivity i.e. S = $\Delta\lambda/\Delta n$, e.g. 8/0.0256, S = 313 nm/RIU (refractive index units).

Table 5.3 lists the characteristics of the gold SPR band of different platforms in water and 2-propanol environments. The results listed in this table were calculated in the same manner as mentioned above.

Batch	Name of the Sample	T °C	λ nm (H_2O)	A (H_2O)	λ nm (i-Pr)	$\Delta\lambda$ nm (i-Pr)	A (i-Pr)	S nm/RIU (i-Pr)
I	C AU	90	530	0.22	535	5	0.2	113
II	2A	82	545	0.32				
	2B	72			550	10	0.35	226
	5A	82	540	0.47	545	7	0.38	158
III	1A	105	550	0.41	555	5	0.54	113
	1A'	-	540	0.77	550	10	0.32	226
	2A	105	555	0.24	560	5	0.77	113
	2A'	-	555	0.3	560	9	0.33	204
	7A	105	550	0.66	565	15	0.56	339
IV	2A	90	542	0.72	550	8	0.63	181
	2B	90	540	0.77	543	3	0.63	68
	5A	90			580		0.72	
	5B	90	538	1.6	545	7	1.15	158
	7A	90	550	0.9	565	15	0.64	339

Table 5.2: Characteristics of Gold SPR band in Water and 2-Propanol

It was observed that the highest sensitivities corresponds to the samples with the smallest hole structures; however sample 7A from table 5.2, which corresponds to a larger sphere size, also shows a high sensitivity (refer to table 4.1 for the corresponding sizes of the PS microspheres). It should also be noted that S is dependant upon the quality of the structures.

Typical spectra corresponding to a film prepared with 700 nm PS spheres, recorded in water and 2-propanol are given in Figure 5.13. The spectrum shows that, by varying the refractive index around the gold nanostructures from 1.333 (water) to 1.377 (2-propanol), i.e. for Δn = 0.044, the gold SPR band shifted by 8 nm to longer wavelengths. This corresponds to a sensitivity of approximately 340 nm·RIU^{-1}, which is higher than the values reported (almost double than that reported in previous work refer to [15]) for gold nanoparticles randomly absorbed from solution. Sensitivities of the same order were found for other samples prepared under different conditions. The shift was lower (~5-7 nm) for the samples prepared with commercial gold (diameter = 20 nm). Although the absorbance of the SPR band showed some changes with the refractive index of the environment, the change was not linear and the results were not reproducible. Some factors that may have contributed to this may be the size distribution of the gold nanoparticles which was not always exactly the same (30 +/-5 nm), the quality of DI water used during the synthesis of the gold.

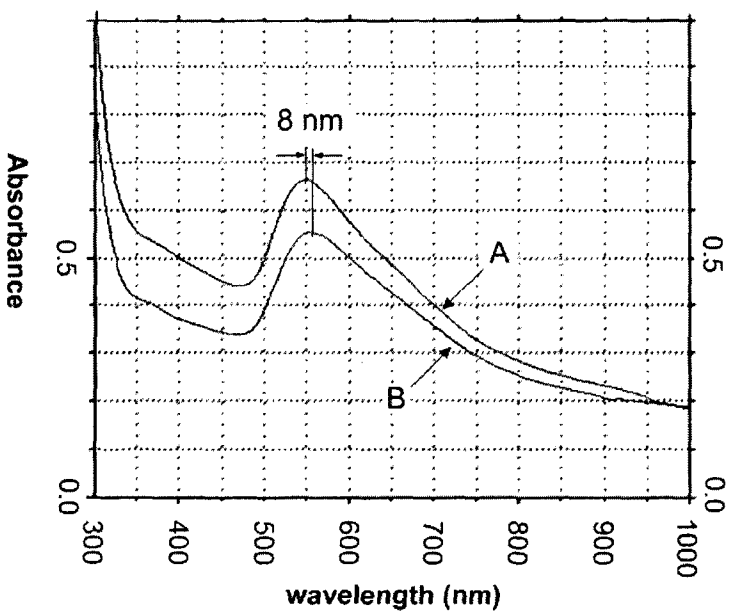

Figure 5.13: The spectrum of a nanohole /nanoring array in water A) and 2-propanol B) (sample annealed for 30 min at 1100°C) [66]

5.3 Biomolecular Interactions

In order to further study the sensitivity of our sensors, the interaction of the samples prepared with the gold nanostructures with a biological macromolecule was also investigated. The following biological molecules were used:

- Fibrinogen
- amyloid β–derived diffusible ligands (ADDL)
- Protein (AT5G07010.1) and its respective antibody

5.3.1 Interaction with Fibrinogen

Prior to taking the measurements, the gold nanostructures were functionalized with 3-MPA and then were incubated with fibrinogen for 24 h at room temperature. Two concentrations of fibrinogen were used for this work; 100 μg/mL and 1000 μg/mL – sensitivity is calculated by using at least two different concentrations. Table 5.4 provides the responses of the sensor platforms to fibrinogen, in PBS; PBS is a buffer solution based on phosphates. This table provides the immediate response i.e. the samples were not incubated for long periods of time in PBS.

Non-Annealed	100 μg/mL	1000 μg/mL	Sensitivity nm/RIU	
	Δλ (nm)	Δλ (nm)	100 μg/mL	1000 μg/mL
1A'	6	6	150	150
2A'	2	1	50	25
Annealed				
2A 90^{0}C, 70 min	-	5	-	125
5A 82^{0}C, 20 min	9	7	225	175

Table 5.3: Sensor Platform Response to Fibrinogen

The value of the refractive index measured is given in the reference [66]. The data provided in Figure 5.14 was used in order to calculate the sensitivity of the platform.

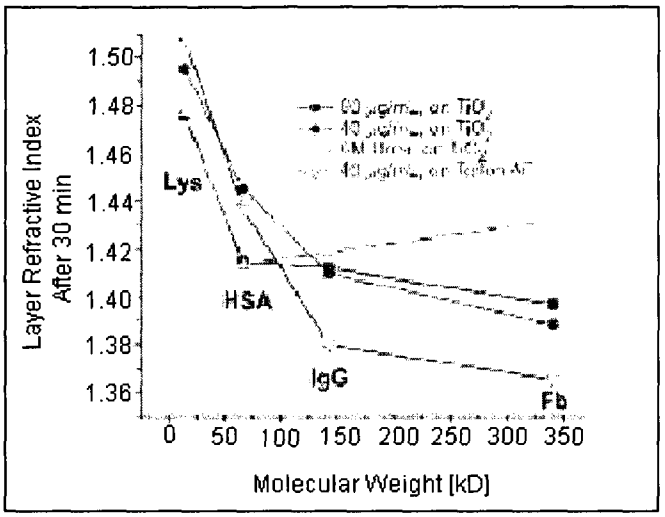

Figure 5.14: Refractive Index of Fribrinogen [66]

The refractive index corresponds to fibrinogen adsorbed on two different substrates (TiO2 – a hydrophilic surface and Teflon – a hydrophobic surface) from solutions having different concentrations. The lowest value of the refractive index (around 1.37, which is an approximation), was chosen for the calculations; the value of S would indeed be higher for higher values of the refractive index. The shift of the SPR band ($\Delta\lambda$) is calculated in a solvent (in this case PBS) compared to water. $\Delta\lambda$ was calculated by subtracting λ in PBS from λ obtained in water. The change in the refractive index, Δn, was 0.04 ($n_{fibrinogen}$ = 1.37 - n_{water} = 1.333). Sensitivity i.e. $S = \Delta\lambda/\Delta n$, e.g. for Sample 5A, 9/0.04, S = 250 nm/RIU (refractive index units).

The platforms fabricated with small spheres show a good sensitivity even for more diluted solutions (100 μg/mL). Since our interest was mainly in the immediate response, the samples were not incubated for long periods of time in PBS. It was observed (not shown in the table) that for the more concentrated solution (1000 μg/mL) there is a change in the absorbance as well. However, the gold nanohole/nanoring structures work as a wavelength shift sensor; this implies that sensitivity is calculated

from the wavelength shift and not the change in absorbance. The results have shown significant shifts for both the fibrinogen solutions (100 and 1000 $\mu g \cdot mL^{-1}$).

5.3.2 Interaction with Amyloid β–Derived Diffusible Ligands (ADDL)

As stated in previous chapters, ADDLs are biologically relevant molecules that may cause neurological dysfunctions. These dysfunctions are related to memory loss, and it is thought, that they may be associated to the development of Alzheimer's disease. The ADDLs were prepared from the following polypeptide; Amylod β 1-42 (A β_{1-42}) according to Lambert's procedure as detailed in chapter 4 [61]. Prior to taking the measurements, ADDL was deposited on the functionalized gold structure and left in contact with the sensor platform for 24 hours. The sensitivity of the SPR band of the functionalized gold nanostructures toward ADDLs was investigated. The results indicated a large shift of the SPR band, as depicted in figure 5.15.

The shift of the SPR band ($\Delta\lambda$) is calculated in a solvent (in this case PBS) compared to water. $\Delta\lambda$ was calculated to be 30 nm. This was calculated by subtracting λ in PBS without any ADDL on the Gold, from λ obtained in PBS with ADDL on the gold.

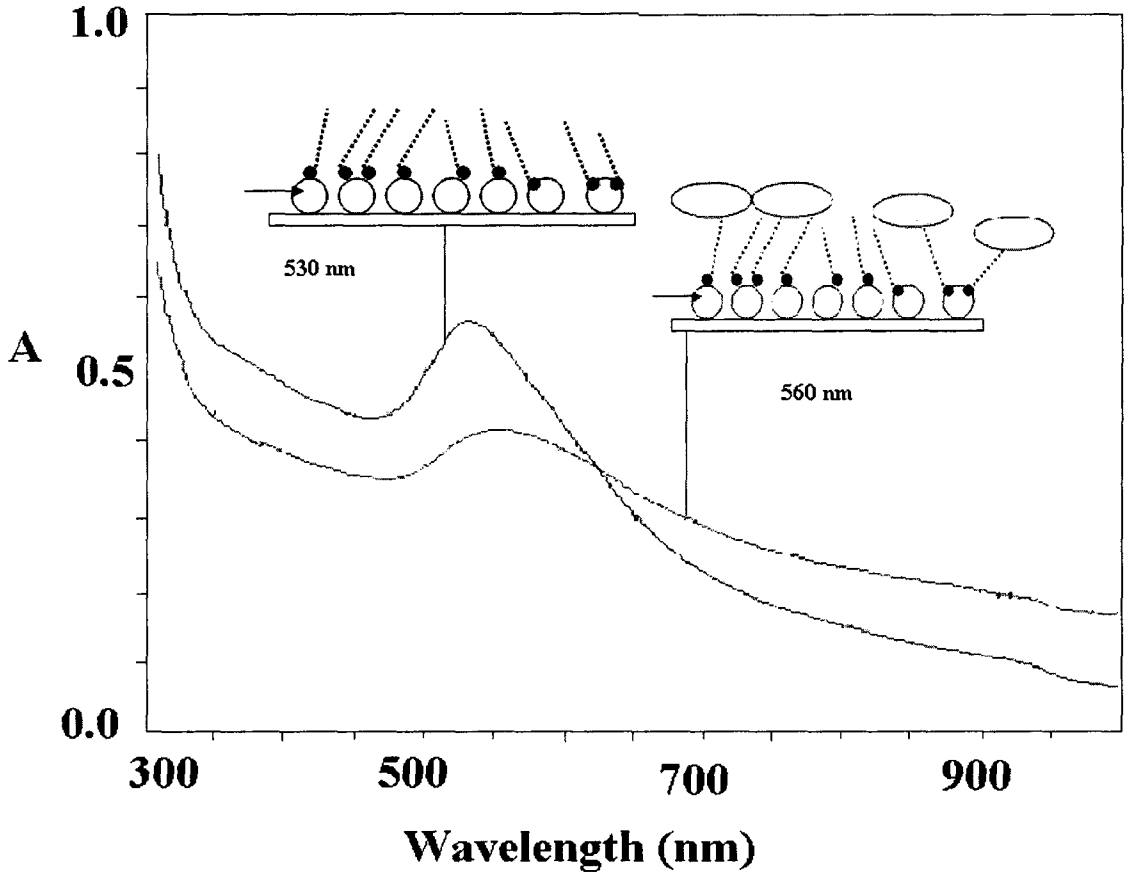

Figure 5.15: UV-VIS spectrum of ADDLs on Gold

5.3.3 Interaction with a Protein (AT5G07010.1) and its Respective Antibody

It can be seen from Figure 5.16 that there is a shift of 10 nm in the SPR absorption of Au, when the antibody is adsorbed. It appears that there is no additional shift after the protein incubation. However the absorption is considerably extended into the longer wavelengths, i.e. a shoulder around 600 nm.

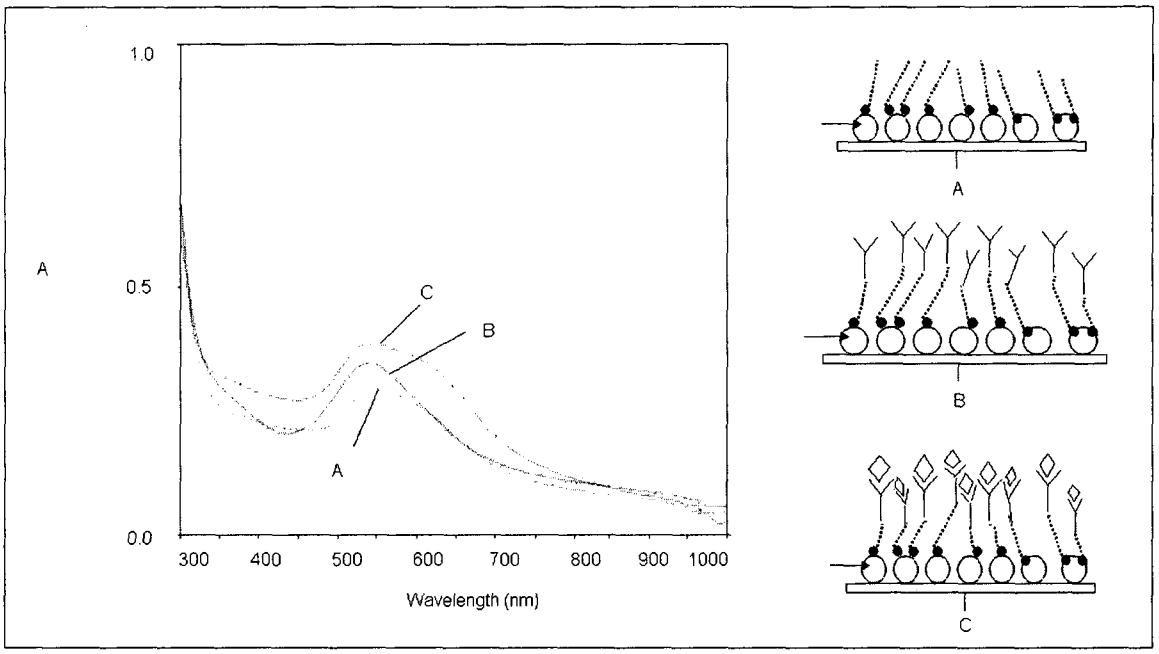

Figure 5.16: Spectra of the protein-antibody interaction: A) spectrum of the functionalized substrate using Au that was prepared in the lab B) spectrum of the antibody adsorbed on the substrate C) spectrum of the previously absorbed antibody followed by the adsorption of the protein on the substrate

Figure 5.17 depicts that when an additional antibody layer is adsorbed on the previous system (sandwiched system), there appears to be shift of around 10 nm in the sandwiched sample and an increase in the absorbance.

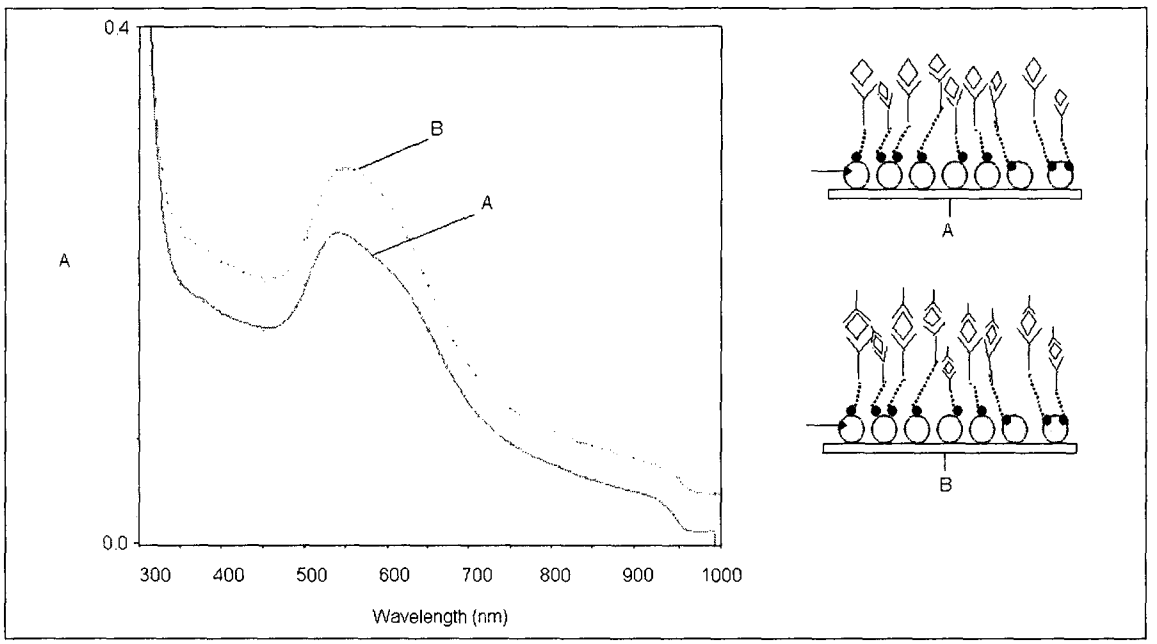

Figure 5.17: Spectrum of the protein sandwiched between two antibody layers: A) Spectrum of the functionalized substrate with antibody and protein adsorption – using Au that was prepared in the lab B) spectrum when an additional antibody layer is adsorbed on the system corresponding to trace A

When the protein, AT5G07010.1, was first incubated on the functionalized gold structure (Figure 5.18b), before the antibody, the Au LSPR band shows a small shift (3 nm), together with the presence of the 600-620 nm shoulder on the broadened band. It should be noted that this shift corresponds to a very low concentration of protein (4.3 x 10^{-7} M), indicating a high sensitivity of the nanohole structure toward this protein. When the antibody is introduced into the system (Figure 5.18 c) there is no further change in the spectrum.

It is hypothesized that there is a change in the size of the gold nanoparticles after the adsorption of the protein and antibody. This would indeed change the properties of the sensor, and this phenomenon is most probably irreversible. The results show that the gold nanostructures are sensitive toward the protein-antibody interaction; this signifies that the gold nanostructures show a biological interaction. Further work is required to quantify this response and to calculate the affinity constant.

Note: The protein and antibody adsorptions were done following the protocol described in chapter 4.

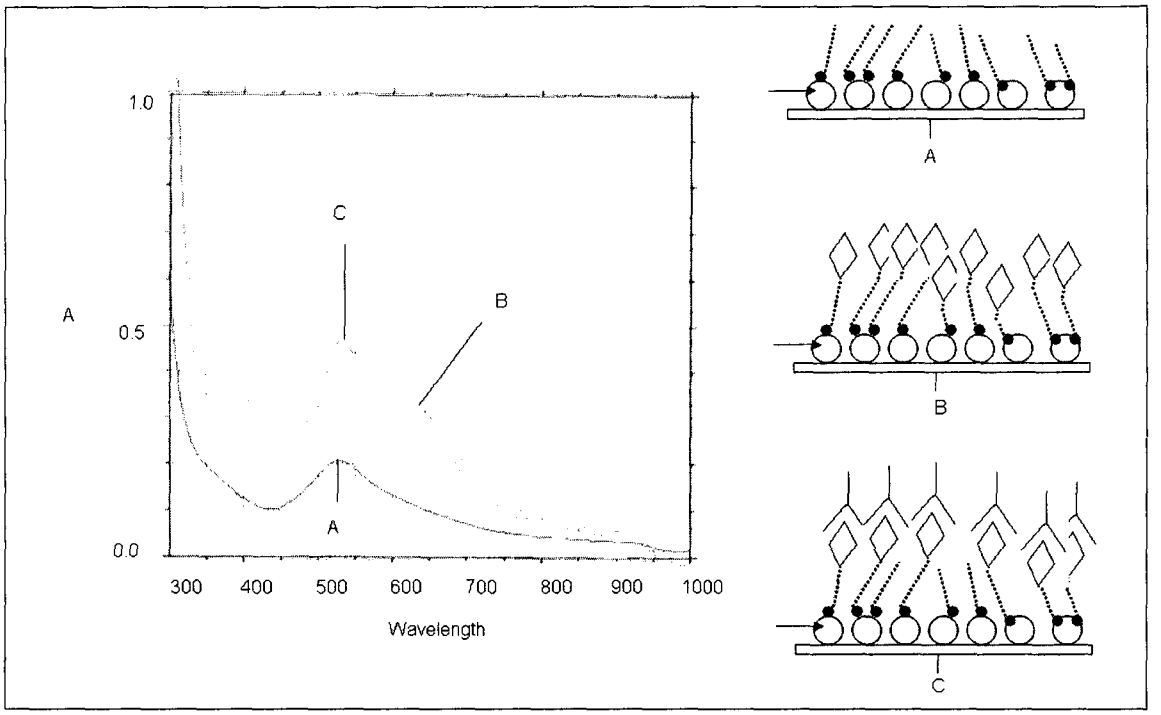

Figure 5.18: Spectrum corresponding to the protein-antibody interaction: A) Spectrum of the functionalized substrate using commercial Au B) Spectrum of the protein adsobed on the substrate C) Spectrum of the previously absorbed protein followed by the adsorption of the antibody on the substrate

Our results show a significant broadening of the Au Plasmon band with a shoulder at 600 nm (this corresponds in one case to the addition of protein and in the other to the addition of antibody to the protein). This is in agreement with Lee and Perez-Luna's [68] results in the case of Concanavalin A's (a sugar-binding protein) interaction with dextran (a polysaccharide). The broadening and the presence of the 600 nm band was accounted for by the aggregation of gold particles attached to dextran upon the interaction with Con A. The aggregation takes place because the gold particles are brought into proximity due to this interaction and their oscillations are coupled. The same phenomenon was found for the streptavidin-biotin pair.

5.4 Raman Characteristics

Raman characteristics were studied to determine whether or not there would be an enhancement in the Raman absorption when introducing a toxin called Saxitoxin (STX) i.e. would the studied bands increase in intensity.

Two toxins were measured on the gold nanostructures. These two toxins have the same basic structure; however the relative position of the radicals is different. They are both very toxic and an analytical method, without a complicated preparation procedure, is required in order to detect these particular toxins. The samples are simply drop-coated on the Au nanoring gold nanostructure, dried and then, measured. Figure 5.19 and 5.20 depicts the structure of this toxin.

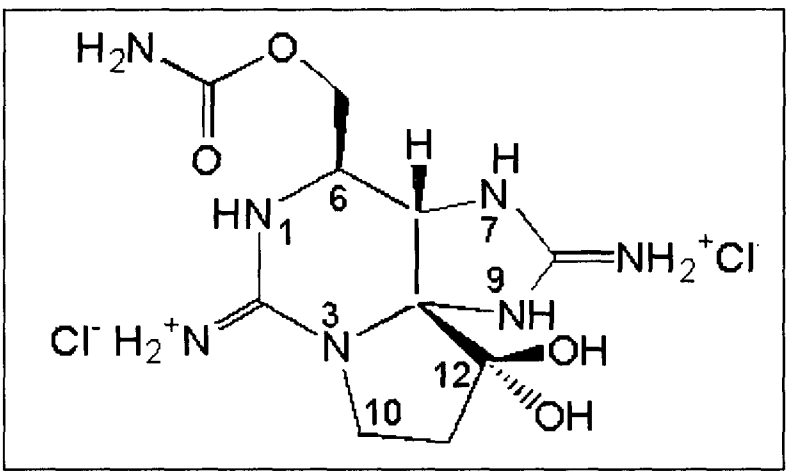

Figure 5.19: Saxitoxin-e (STX-e) [69]

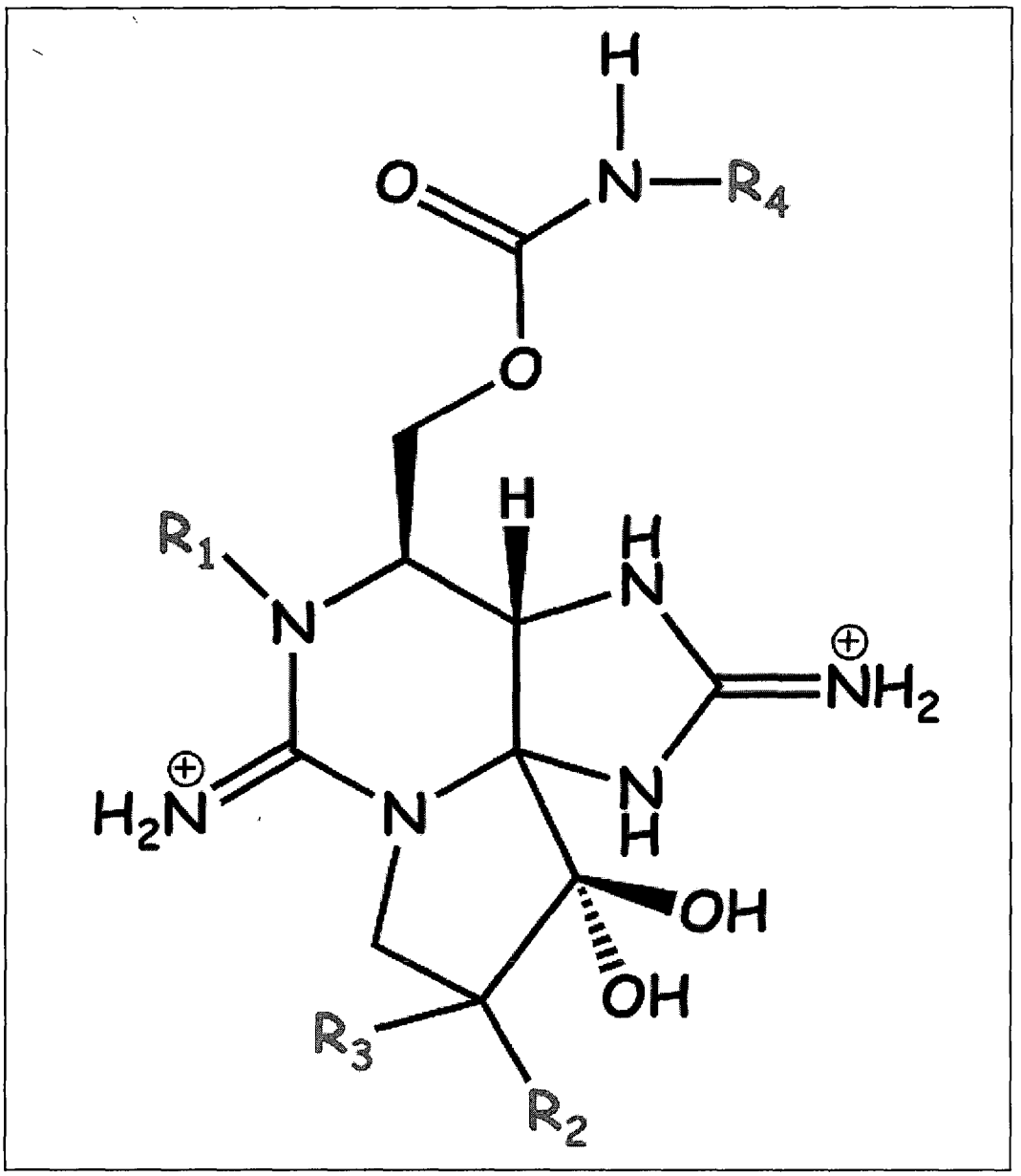

Figure 5.20: Gonyautoxin (Paralytic Shell Fish Poisoning toxin) [69]

The Raman signature of Saxitoxin is located at 988 cm^{-1}. This is a highly intense mode and can be used for the detection of Saxitoxin-e. After lyophilisation a solid particle of STX was obtained and it was used as the reference for the Raman signal (Figure 5.21d). In order to identify the regions which contribute to the intense Raman signal, two dimensional mapping on the samples were performed. The two dimensional mapping was performed over 35x25 μm within a cell size of 7x5 microns. Figure 5.21

shows the Raman spectra from the selected locations where there is an intense signal. Three samples were analyzed in this particular trial, each with varying exposition times.

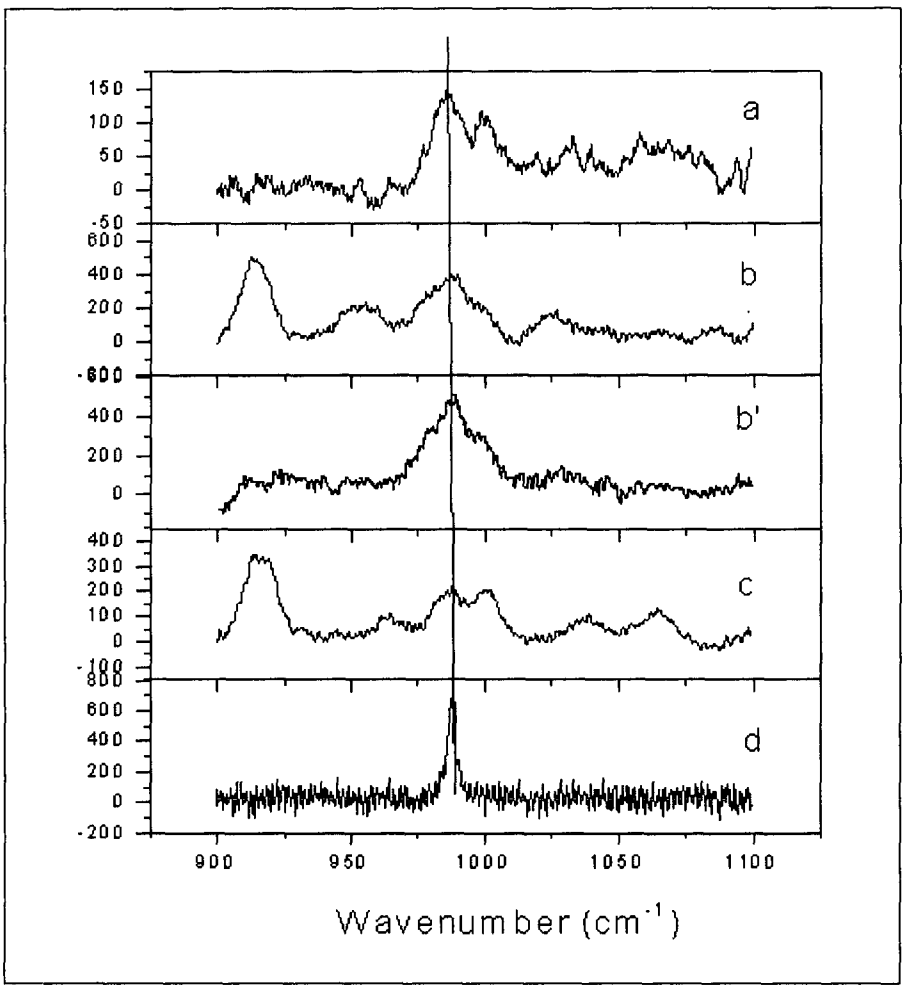

Figure 5.21: Raman Spectra of samples – a) sample a, b) sample b, b') sample b with different exposition time, c) sample c, d) STX-Solid-Reference

Table 5.5 presents all the obtained enhancements for the analyzed samples for the obtained spectras.

S.No	Sample Name	Obtained Intensity for 988 cm-1 mode	Exposition time (sec)	Intensity (counts/sec)	Intensity Correction for optical density filter	Intensity In the comparable scale	Enhancement factor
1	a	137	5	27	10	275	37
2	b	380	10	38	4	152	21
3	b'	500	10	50	4	200	27
3	c	221	20	11	4	44	6
4	d	665	90	7	1	7	1

Table 5.4: Raman Enhancements

When comparing all the samples to the STX Solid Reference there is an enhancement of about 37 time for sample a, 27 and 21 times for sample b' and b respectively, and only 6 times for sample c. The signal from STX-e was identified by the position of 988 cm^{-1} peak. The broadening of the peaks may be attributed to the dried STX-e; dried STX-e has a narrower line width compared to the ones obtained from the solution form of STX-e. Furthermore, the peak of 1002.9 from the PS spheres overlap with the STX-e peak position; this may have also contributed to the broadening of the peaks.

An additional sample was also analyzed for this study. Figure 5.22A shows the Raman spectrum of the analyte (STX) on a glass substrate. The Raman spectrum of an unannealed nanoring structure is shown in Figure 5.22B with the corresponding white light optical microscopic image (Figure 5.22D). The white light optical microscopic image of the edge of a dried drop-coated STX solution on an unannealed nanoring is shown in Figure 5.22E. After drying, many STX crystallites were formed on the surface of the nanorings (Figure 5.22E) and the Raman spectra were recorded where the crystallites were seen, using the point acquisition mode. It can be seen that the background signal from the unannealed nanostructure (lower trace) was very low when compared to that obtained from the drop-coated STX. The mode located at 988.4 cm-1 corresponding to the stretching vibrations of C-N bonds located at the 7, 8, 9, and 1, 2, 3 positions of the

STX, is clearly seen. The intensity of the Raman signal from the STX on the unannealed nanorings was compared to that on glass substrate and it was found that the enhancement was around 4.6 times.

Figure 5.22C shows the Raman spectra of annealed sample (lower trace) and of the dried STX (upper trace). In this experiment, two dimensional Raman mapping was carried out and the data originate from the hot spot. The enhancement factor of the Raman mode at 988 cm-1 is found to be 7 compared to the Raman spectrum of the STX on a glass substrate. The white light optical microscopic images of the annealed sample, as well as that of the drop-coated STX solution are similar to Figure 5.22E and Figure 5.22D, respectively. In both spectra (Figure 5.22B and Figure 5.22C), we found that the Raman line is broadened when compared with that of the powder STX. In this work, the signal from STX was identified by the position of the peak. The broadening of the peaks could be attributed to the STX dried from the solution.

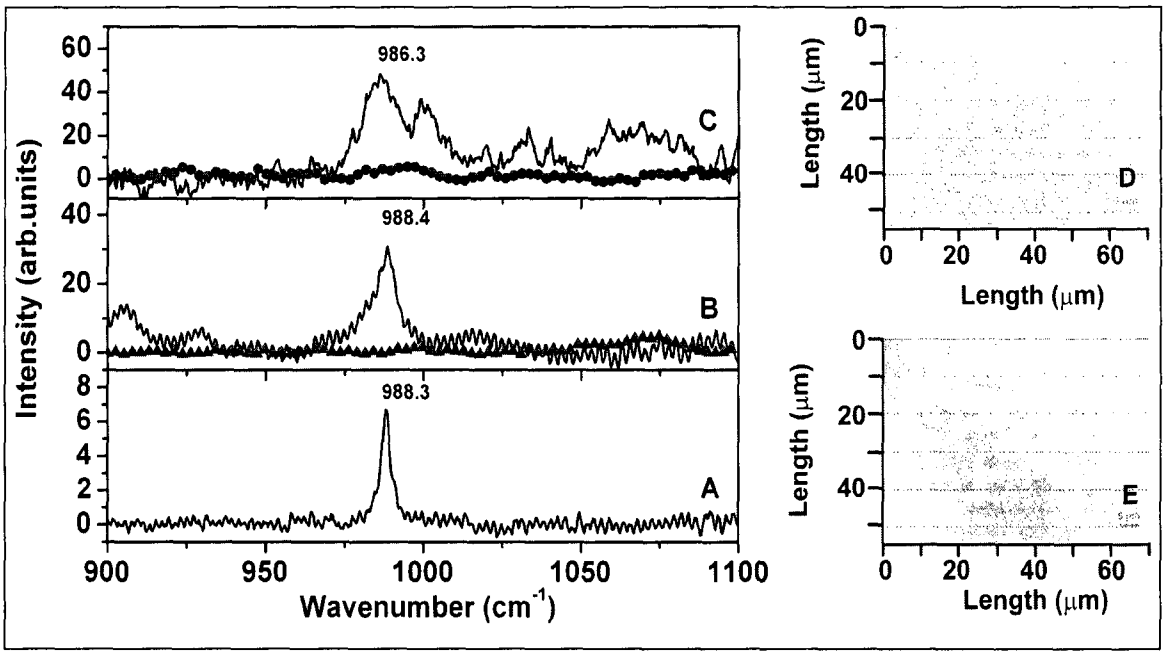

Figure 5.22: Raman spectra of the nanohole/nanoring structures: A) the analyte (STX) on a glass substrate, B) the unannealed nanostructure (lower trace) and the analyte (STX) on the unannealed structure (upper trace), C) the annealed nanostructure (lower trace) and the analyte (STX) on the annealed structure (upper trace). D) White light optical microscopic image of the unannealed nanostructure. E) White light optical microscopic image of the analyte (STX) dried on the unannealed nanostructure [66].

To summarize it has been observed that, while the enhancement factors are not too high they are enough to permit the detection and identification of the toxins.

Gold nano-hole and nano-ring structures have proved to be SERS (Surface-Enhanced Raman Scattering) active surfaces. In addition to this, the characteristic Raman bands (fingerprints) collected from the toxin immobilized on the Au nanostructures enables the highly specific detection of marine toxins. Finally, different toxins can be identified individually.

Chapter 6 : Conclusion and Contribution

In this work new nanostructures have been prepared, i.e nanoholes and nanoring structures, by a modified nanolithography method. Polystyrene-gold nanoparticle composites were deposited by self-assembled deposition, on a silane-activated glass substrate. The composite was then annealed under various conditions, in order to allow the formation of ring structures. Once the polystyrene microspheres were removed, by dissolution in ethanol, a uniform well ordered structure was obtained.

The sensing properties of these nanostructures have been studied by using organic solvents, and biomolecules. The sensitivity of the nanostructures for acetone and 2- propanol was found to be around 200-400 nm/RIU, depending upon the geometrical characteristics of the nanostructures. The sensitivity calculated for fibrinogen was determined to be 250 nm/RIU. A large shift of 30 nm (which implies a high sensitivity) was observed towards ADDL when this biomolecule was adsorbed onto the functionalized substrate, which may be attributed to the prolonged incubation time.

A biomolecular interaction was also observed for the sensor platform, by using a protein called AT5G07010.1, and its corresponding antibody. This protein is found in Arabidopsis; a small flowering plant related to cabbage and mustard. It is one of the model organisms used for studying plant biology and the first plant to have its entire genome sequenced. The specific interaction between the protein and antibody resulted in a shift of around 10 nm. An extended absorption, with a maximum of around 600 nm, was also observed. It is believed that the extended absorption is due to a change in the size of the gold nanoparticles and aggregates after the adsorption of the protein and antibody. Further work is required in order to determine the mechanism of the protein antibody interaction on our particular nanostructure.

To summarize, this technique has the advantage of simplicity; the structures can be prepared without any special equipment and a standard cell can be used for optical measurements. A UV-vis spectrophotometer was used for the optical detection; however a fiber optics spectrometer could also have easily been used to further reduce the cost of equipment. In addition to this, it provides the possibility of real-time analysis of bimolecular interactions without the need of labeled molecules with only a small sample. The analysis of the biomolecular interaction is completed within a few minutes, and it is possible to re-use the sensor platform after surface regeneration (desorption of the protein-antibody with the use of PBS).

Future work requires further quantification of the biomolecular interaction in order to calculate the protein-antibody affinity constant. Furthermore, the self-assembled monolayers used to functionalize the substrate will have to be diversified. In addition to 3-Mercaptopropionic acid used in this study, molecules with longer alkyl chains should be used together with more hydrophobic SAMs. Different SAMs or mixed SAMs (hydrophobic with hydrophilic molecules) would improve the accessibility of the proteins to the surface by reducing the steric hindrance and improving the immobilization of the protein on the surface (the bulky head groups prohibit the access of the proteins to the surface). The sensitivity towards other classes of chemical compounds of interest e.g. narcotics should also be investigated. To further determine the parameters of the sensor platform, it is recommended that a flow cell be used during the adsorption of the protein and antibody. With a flow-cell, will control and the amount of solution introduced could be controlled, and it also provides time control, which would further enhance accuracy during the measurements. Furthermore, during the desorption process, a flow cell would enable the monitoring of the signal to ensure that the adsorbed layer is fully removed, in order to re-use the same sensor platform for further tests.

The key contributions made during the course of this research are the following:

- A SPR biosensor using gold nanoparticles immobilized on optically transparent substrates was developed. Sensing was conducted using absorbance mode as opposed to the reflection mode stipulated as part of the Kretchmann configuration.
- Array (nanohole and nanoring structures were prepared without using any expensive lithographic method generally used to fabricate for example, protein array structures. An array structure is obtained using special lithographic techniques e.g. e-beam method; these methods are expensive. Our method resulted in arrays without the use of these complex and expensive techniques.
- Annealing of the composite samples in order to obtain nanoring structures – the high temperature allowed for the Au nanoparticles to move and form rings around the holes; this was completed in order to further study bimolecular interactions.
- Study of the dependency of the sensitivity of the sensor platform to the size of the nanoholes/nanoring structures – platforms fabricated with smaller polystyrene microspheres resulted in increased sensitivity; smaller spheres resulted in an increased number of binding sites for the biomolecules.
- A protein from a plant was used in order to build a model system, which is not generally used in other research work – most researchers used fibrinogen, BSA or EIM-immunoglobulin as a model protein in order to investigate bimolecular interactions on a sensor of this nature. The plant protein used in our study is quite large. This protein was not purchased, it was synthesized with the help of biological experts in this domain
- ADDL was also used to study the characteristics of the sensor platform. ADDL is not a model protein and was used for this research due to its possible link to Alzheimer's disease. It is a very complex and expensive protein. ADDL was

prepared from the polypeptide Amyloid β 1-42 (A β 1-42) in two steps; Monomerization (polymer that defragments into monomers) by HFIP and storage of Aβ peptide is first required, followed by the preparation of ADDL. This procedure was completed with the assistance of biological experts. For future studies, it is recommended to further study the interaction of this protein with the sensor platform, however the equivalent antibody should also be obtained in order to fully analyze whether or not this sensor platform can be helpful in the diagnosis of this disease.

References

1. X. Jiang, Q. Zeng, and A. Yu, Nanotechnology, **17**, 4929 (2006).
2. Y. Sun, and Y. Xia, Anal. Chem., **74**, 5297 (2002).
3. J. S. Shumaker-Parry, H. Rochholz, and M. Kreiter, Adv. Mater., **17**, 2131(2005).
4. C. L. Nehl, H. Liao, and J. H. Hafner, Nano Lett., **6**, 683 (2006).
5. Y. Chen, X. Gu, C.-C. Nie, Z.-Y. Jiang, Z.-X. Xie, and C.-J. Lin, Chem. Commun., **1359-7345**, 4181 (2005).
6. E. M. Larsson, J. Alegret, M. Käll, and D. S. Sutherland, Nano Letters, **7**, 1256 (2007).
7. J. Aizpurua, P. Hanarp, D. S. Sutherland, M. Käll, G. W. Bryant, and F. J. Garcia de Abajo, Phys. Rev. Lett., **90**, 57401 (2003).
8. P. Hanarp, D. S. Sutherland, J. Gold, and B. Kasemo, Nano Structured Materials, **12**, 4432 (1999).
9. D. Jia, and A. Goonewardene, Appl. Phys. Lett., **88**, 531051 (2006).
10. A. Kosiorek, W. Kandulski, H. Glaczynska, and M. Giersig, Small, **1**, 439 (2005).
11. S. -M. Yang, S. G. Jang, D. -G. Choi, S. Kim, and H. K. Yu, Small, **2**, 458 (2006).
12. Y. B. Zheng, S. J. Wang, A. C. H. Huan, and Y. H. Wang, J. Appl. Phys., **99**, 034308 (2006).
13. S. Kim, J. -M. Jung, D. -G. Choi, H. -T. Jung, and S. -M. Yang, Langmuir, **22**, 7109 (2006).
14. A. De Leebeeck, L. K. S. Kumar, V. De Lange, D. Sinton, R. Gordon, and A. G. Brolo, Anal. Chem., **79**, 4094 (2007).
15. N. Nath, and A. Chilkoti, Anal. Chem., **74**, 504 (2002).
16. N. Nath, and A. Chilkoti, Anal. Chem., **76**, 5370 (2004).

17. N. Nath, and A. Chilkoti, J. Fluorescence, **14**, 377 (2004).

18. A. L. Weikel, S. D. Conklin, J. N. Richardson, Sensors and Actuators B: Chemical, **110**, 112 (2005).

19. F. Frederix, J. -M. Friedt, K. -H. Choi, W. Laureyn, A. Campitelli, D. Mondelaers, G. Maes, and G. Borghs, Anal.Chem., **75**, 6894 (2003).

20. G. Kalyuzhny, A. Vaskevich, M.A. Schneeweiss, I. Rubinstein, Chem. Eur. J., **8**, 3850 (2002).

21. M. Lahav, A. Vaskevich, I. Rubinstein, Langmuir, **20**, 7365 (2004).

22. I. Doron-Mor, H. Cohen, Z. Barkay, A. Shanzer, A. Vaskevich, I. Rubinstein, Chem. Eur. J., **11**, 5555 (2005).

23. A. J. Haes, W. P. Hall, L. Chang, W. L. Klein, and R. P. Van Duyne, NanoLetters, **4**, 1029 (2004).

24. A. D. Ormonde, E. C. M. Hicks, J. Castillo, and R. P. Van Duyne, Langmuir, **30**, 6927 (2004).

25. R.P. Van Duyne, J. C. Hulteen, and D.A. Treichel, J. Chem. Phys., **99**, 2101 (1993).

26. J. C. Hulteen, D. A. Treichel, M. T. Smith, M. L. Duval, T. R. Jensen, and R. P. Van Duyne, J. Phys. Chem. B., **103**, 3854 (1999).

27. S. Badilescu, M. Kahrizi, P. V. Ashrit, and V. -V. Truong, in Proc. Nanotech Conf., 293 (2006).

28. Y. Djaoued, S. Badilescu, S. Balaji, N. Seirafianpour, A. R. Hajiaboli, R. Banan Sadeghian, K. Braedley, R. Brüning, M. Kahrizi, and V. -V. Truong, Appl. Spectrosc., **61**, 1202 (2007).

29. D.A. Stuart, A.J. Haes, C.R. Yonzon, E.M. Hicks and R.P. Van Duyne, IEE Proc.-Nanobiotechnol, **152**, 13 (2005)

30. T. Vo-Dinh, B. Cullum, Anal. Chem., **366**, 540 (2000)

31. X. Hong and F.-J. Kao, App. Optics, **43** (14), 2868 (2004)

32. A. Dahlin, Exploitation of the Void Development of a Nano-Optical Biosensor, (Lund University, Lund, 2006)

33. A.J. Haes, W. P. Hall, L. Chang, W.L. Klein, and R.P. Van Duyne, Nano Lett., **6**, 1029 (2004)

34. P. Torreri, M. Ceccarini, P. Macioce and T.C. Petrucci, Ann Ist Super Sanità, **41**, 437 (2005)

35. N. Nath and A. Chilkoti, J. Fluorescence, **14**, 377 (2004) –

36. K. Willets and R.P. Van Duyne, Annu. Rev. Phys. Chem., **58**, 267 (2007)

37. http://en.wikipedia.org/wiki/Mie_scattering (August 11, 2008 - 2 am)

38. Z. Mondona, R. Terril, Surface Plasmon spectra of silver and gold nanoparticle assemblies, Dekker Encyclopedia of nanoscience and nanotechnology, 1:1, 3819-3830 (2004).

39. E. Hutter, J.H. Fendler, Exploitation of Localized Surface Plasmon Resonance, Adv. Mater. 2004, 16, 1689-1706

40. M.D. Malinsky, K. L. Kelly, G.C. Schatz, R.P. Van Duyne, J. Phys. Chem.B, **105**, 2343 (2001)

41. X. Chen and K. Jiang, Nanotechnology, **19,** 1 (2008)

42. J. J Gray, Cur. Opi. Struc. Bio., **14**, 110 (2004)

43. C.E. Hall, H.S.J Slayter, Biophys. Biochem. Cytol., **5**, 11 (1959)

44. K.C. Popat, S.Sharma, R.W. Johnson and T.A. Desay, Surface Interface Anal., **35**, 205 (2003)

45. http://en.wikipedia.org/wiki/Fibrin (October 6, 2008 - 10:25 pm)

46. http://en.wikipedia.org/wiki/Antibody (August 11, 2008 - 2 am)

47. A. Kausaite, M. Van Dijk, J. Castrop, A. Ramanaviciene, J.P. Baltrus, J. Acaite, and A. Ramanavicius, Bio. Molec. Bio Edu., **35**, 57 (2007)

48. M. Clark, Antibody-Antigen Reactions, (Department of Pathology, University of Cambridge)
49. http://en.wikipedia.org/wiki/Scanning_electron_microscope (July 18, 2008 - 10 am)
50. Hitachi S-4700 SEM Training & Reference Guide January 2007
51. http://en.wikipedia.org/wiki/Spectrophotometry (July 20, 2008 - 10 am)
52. http://www.varianinc.com/cgi-bin/nav?products/spectr/uv/cary5000/cary_5000&cid=JMPIINJLFI (July 21, 2008 – 2 pm)
53. http://www.ruf.rice.edu/~bioslabs/methods/protein/spectrophotometer.html (July 21, 2008 - 4 pm)
54. http://course.lib.uci.edu/~mcbrown/xpowder.html (July 21, 2008 - 10 am)
55. http://en.wikipedia.org/wiki/Raman_spectroscopy (July 21, 2008 - 2 pm)
56. E. Smith, in Modern Raman Spectroscopy: A Practical Approach, edited by G. Dent (John Wiley, Hoboken, NJ, 2005).
57. H. Baranska, in Laser Raman Spectrometry, Analytical Application, edited by A. Labduzinska and J. Terpinski (John Wiley, New York, 1987).
58. S. Badilescu, N. Seirafianpour, A. –R. Hajiaboli, Y. Djaoued, M. Kahrizi, P. Ashrit, V. –V. Truong, J. of Materials Science: Materials in Electronics,**18**, 383 (2007)
59. J. Kimling, M. Maier, B. Okenve, V. Kotaidis, H. Ballot, and A. Plech, J. Phys. Chem. B, **110**, 15700 (2006)
60. A. Ulman, Chem. Rev., **96**, 1533 (1996) Figure 4.3
61. W.L. Klein, Neurochem. Inter., **41,** 345 (2002)
62. Qiagen, The QIAexpressionist - A handbook for high-level expression and purification of 6xHis-tagged proteins, Fifth Edition, (Qiagen, 2003)
63. M. M. Bradford, Anal. Biochem., **72**, 248 (1976)

64. Laemmli, Nature, **227**, 680 (1970)

65. Y. Djaoued, S. Badilescu, S. Balaji, N. Seirafianpour, A.-R. Hajiboli, R.B. Sadghian, K. Braedley, R. Bruning, M. Kahrizi and V. –V. Truong, Appl. Spectrosc., **61**, 1202 (2007)

66. F. Fida, R. B. Sadeghian, A.-R. Hajiaboli, Y. Djaoued, S. Badilescu, S. Balaji, M. Kahrizi, and V. –V. Truong, Proceeding of the International Conference on Biocomputation, Bioinformatics, and Biomedical Technology, Romania, Bucharest, 114 (2008)

67. J.Voros, Biophysical Journal, **87**, 553 (2004)

68. S. Lee, V.H. Perez-Luna, Anal. Chem., **77**, 7204 (2005)

69. F. Fida, A. –R. Hajiboli, R.B. Sadeghian, Y. Djaoued, S. Badilescu, S. Balaji, M. Kahrizi, V. –V. Truong, The Thirteenth Canadian Semiconductor Technology Conference, Montreal, Canada, **13**, 89 (2007)

Appendix A: Protein and Antibody Preparation

Expression of recombinant AT5G07010.1 (Protein):

An aliquot of 250 µl of an overnight culture of the *E. coli* strain XLI-blue harboring the AT5G07010.1 cDNA cloned in the expression vector pQE30 served to inoculate 10 ml Luria-Bertani medium. This gene AT5G07010.1 encodes an hydroxyjasmonate sulfotransferase AT5G07010.1. The cells were grown at 30°C for 3 h, before the addition of the inducer, isopropylthio-P-D-galactopyranoside to 1 mM, and incubation was continued for an additional 3 h. Cells were pelleted by centrifugation and suspended in 1 ml 50 mM sodium phosphate, pH 8.0, 0.3 M NaCl and 14 mM 2-mercaptoethanol, and lysed by sonication. Cell debris was removed by centrifugation at 12000 xg for 15 min at 4°C, and the supernatant was applied to 50 µl Ni-nitrilotriacetic acid resin (Qiagen) equilibrated in the same buffer. The resin was washed three times with 1 ml 5 mM sodium phosphate, pH 6.0, 0.3 M NaCl and 14 mM 2-mercaptoethanol, and the proteins were eluted with 250 µl of the same buffer containing 150 mM imidazole. Proteins were measured by the method of Bradford [63], and bovine serum albumin was used as the standard protein.

Antibody Production:

In order to get a protein preparation of high purity for antibody production, Ni-nitrilotriacetic acid resin-purified recombinant AtST2a was further purified by affinity chromatography on a 3'-phosphoadenosine 5'-phosphate agarose resin. The bound protein was eluted using a linear gradient of salt and the elution was monitored using absorbance at 280 nm. The purity of the preparation was tested by gel electrophoresis under denaturing conditions according to the method of Laemmli using 12%

polyacrylamide gels [64]. The molecular weight of the purified protein (41,000 Dalton) was found to correspond to the predicted molecular weight of the recombinant protein.

New Zealand rabbits were immunized according to the following schedule: 80 µg of purified recombinant AT5G07010.1 was mixed with complete Freund's adjuvant (1:1, v/v) and injected subcutaneously at days 1, 21, 42, and 63. The rabbits were bled from the marginal ear vein before immunization (pre-immune serum), and prior to booster injections. Sera were separated from red blood cells by clotting the red cells overnight at 4^0C, followed by centrifugation at 10,000 x g in a clinical centrifuge. The serum titer was verified by ELISA. At day 87, the rabbits were anaesthetised and their blood collected by cardiac puncture. A serum dilution of 1:1000 (v/v) was used in subsequent immunological methods.